LHCb-PUB-2014-015
LHCb-INT-2013-004
February 25, 2014

Viability Assessment of a Scintillating Fibre Tracker for the LHCb Upgrade

A. Bay[10], F. Blanc[10], S. Bruggisser[10], O. Callot[2], H. Chanal[1] E. Cogneras[1], A. Comerma-Montells[8], M. Deckenhoff[3], G. Decreuse[9], M. Demmer[3], V. Egorychev[5], R. Ekelhof[3], D. Gascon[8], A. Golutvin[11,5,9], E. Graugés[8], O. Grünberg[12], E. Gushchin[6], Yu. Guz[7], G. Haefeli[10], P. Jaton[10], C. Joram[9], M. Karacson[9], B. Leverington[4], R. Lindner[9], N. Lopez-March[10], T. Nakada[10], M. Patel[11], P. Perret[1], A. Puig Navarro[10], B. Rakotomiaramanana[10], J. Rouvinet[10], T. Savidge[11], O. Schneider[10], T. Schneider[9] P. Shatalov[5], B. Spaan[3], E. Thomas[9], G. Veneziano[10], U. Uwer[4], Z Xu[10], H. Yu[10].

[1] *Université Blaise Pascal, Clermont-Ferrand, France,* [2] *LAL, Université Paris-Sud, Orsay, France,* [3] *Technische Universität Dortmund, Germany,* [4] *Ruprecht-Karls-Universität Heidelberg, Germany,* [5] *ITEP, Moscow, Russia,* [6] *INR RAN, Moscow, Russia,* [7] *IHEP, Protvino, Russia,* [8] *Universitat de Barcelona, Spain,* [9] *CERN, Geneva, Switzerland,* [10] *EPFL, Lausanne, Switzerland,* [11] *Imperial College London, United Kingdom,* [12] *Universität Rostock, Germany*

Abstract

This document describes the parameters and qualities of scintillating fibres and silicon photodetectors for a central tracking detector for the LHCb upgrade and discusses the viability of the proposals for a tracking detector set forth in the Framework Technical Design Report and Letter of Intent. It summarizes experimental, simulation and literature studies to assess the viability of the baseline components with a particular emphasis being put on their tolerance to damage from radiation. The specifications of the fibre and photodetector will have strong impact on the design of the front-end electronics and vice versa. Some of the results for this are also reported here. Finally, we will present a conclusion based on the results of our studies and other collaborations, regarding the suitability of a scintillating fibre based tracker with a Silicon Photo-Multiplier (SiPM) read out in the higher luminosity environment of the upgrade scenario.

Contents

1 Introduction

The primary goal of LHCb is to measure the effects of new particles or forces beyond the Standard Model. Results obtained from data collected in 2010 have shown that the detector is robust and continues to function as expected. While LHCb will be able to measure a host of interesting channels in heavy flavour decays in the upcoming few years, a limit of about $2\,\text{fb}^{-1}$ of data per year cannot be overcome without upgrading the detector. An upgraded detector, read out at 40 MHz, with a much more flexible software-based triggering strategy, will allow for a large increase not only in data rate, as the detector would collect 5–10 fb^{-1} per year, but also the ability to increase trigger efficiencies, especially in decays to hadronic final states, possibly by a factor of two.

In March 2011 a Letter of Intent (LoI) for the upgrade of LHCb was submitted which outlined the detector concepts, operating environment and new possible areas of physics exploration [1]. A second document, the Framework Technical Design Report (FTDR) [2], added additional details to the LoI and included updates to the detector requirements in anticipation of individual sub-system TDRs. The foreseen environment of the LHC upgrade, as stated in the FTDR, will be as follows:

- LHC collisions will be at $\sqrt{s} = 14$ TeV , with heavy flavour production cross-sections scaling linearly with $\sqrt{s}$.
- the instantaneous luminosity in LHCb will be $L_{inst} = 1 \times 10^{33}$ $\text{cm}^{-2}\text{s}^{-1}$: this will be achieved with 25 ns separation between bunches and up to four interactions per beam crossing;
- LHCb will change the polarity of its dipole magnet with similar frequency as in 2011/12 data taking, to equalise the amount of data taken with each polarity for better control of potential systematic biases;
- the annual integrated luminosity will be $L_{int} = L_{inst} \times t_{\text{LHC}} = 1 \times 10^{33}$ $\text{cm}^{-2}\text{s}^{-1} \times 5 \times 10^{6}$ s $= 5$ fb^{-1} (where the expected LHC annual operational time t_{LHC} is consistent with current experience);
- the upgraded experiment will collect a total sample of $50\,\text{fb}^{-1}$.

In the LoI, the roles of the tracking detectors in LHCb and their performances in the current experiment were presented. The main challenges for the LHCb upgrade were described and a number of exploration paths have been outlined. The current experience with the LHCb detector and preliminary Monte-Carlo simulation results show that the occupancy in the inner area (near the beam pipe) will become too large for the most central Outer Tracker (OT) straw tube modules at the LHCb upgrade luminosity.

This document will focus on the Outer Tracker upgrade and its partial or total replacement called the Central Tracker (CT). In the CT option, the Inner Tracker (IT) and several (or all) Outer Tracker (OT) modules are replaced by new scintillating fibre based modules. An alternative solution, the larger IT option, which we will call IT_+ here,

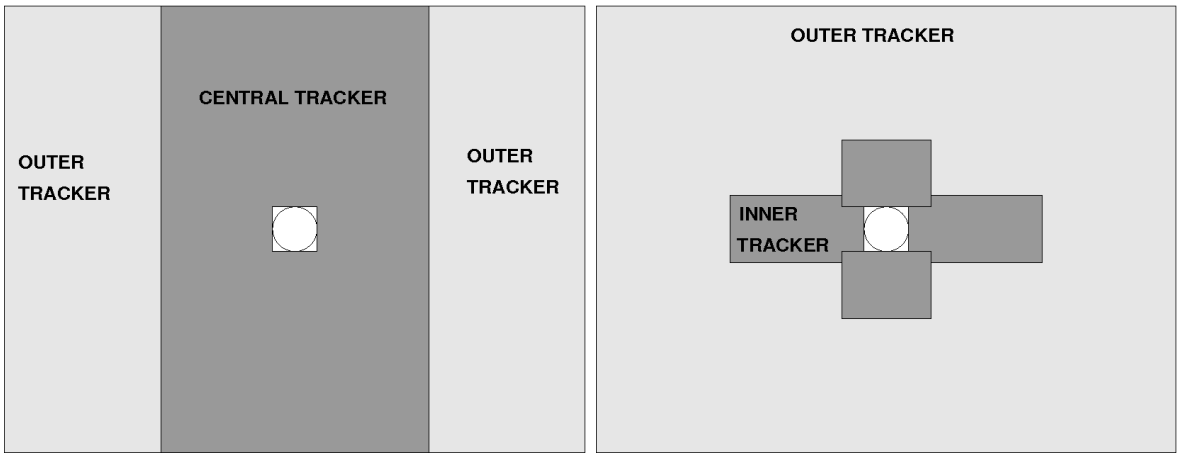

Figure 1: Schematic layouts of the two options being studied for the upgrade of the LHCb tracking stations (not to scale). The CT option with OT straw tubes (light grey area) and scintillating fibre modules (dark grey area) are seen on the left side. The IT_+ option is seen on the right. The central hole is for the beam pipe.

is being explored in parallel and proposes to cover an area larger than the current IT with silicon microstrip sensors and use shorter OT modules for the rest of the acceptance region. The two options (CT and IT_+) are illustrated in Fig. 1.

After the LoI, a few points were reconsidered for the FTDR. The main changes were the following:

- The current LHCb Tracker stations are composed of an OT with straw tube detectors and an IT with silicon strip detectors to cover the high-occupancy area near the beam pipe. The new technology for the OT & IT upgrade, based on scintillating fibres, was introduced in the LoI, with clear fibres carrying the signal photons from the inner region to the detectors situated outside the LHCb acceptance. In the FTDR, a new scintillating-fibre layout has been proposed, with 2.5 m long fibres covering the whole central region of the tracker stations, from the LHC beam plane all the way to the top and bottom of the LHCb acceptance. In this CT option, the IT and several (or all of the) OT modules are replaced by the new scintillating-fibre modules.

- The decision has been taken that any change to the LHCb detector should be made such that the new implementation is compatible with operation at a levelled, i.e. constant, luminosity of 2×10^{33} cm^{-2}s^{-1}.

Both solutions foresee the presence of straw-tube modules to cover the remaining detection area (with the IT_+ solution requiring the additional production of shorter straw-tube modules). All remaining straw-tube modules will be equipped with new front-end and readout electronics compatible with 40 MHz data acquisition, as described in detail in the LoI. Replacing the entire OT with a Fibre Tracker (FT) could also be a possibility with

the advantage of reducing the number of stations and infrastructure to be upgraded or maintained, along with facilitating event reconstruction and reducing associated computing costs. In the performance expectations mentioned later in this note, the FT option is assumed.

In both the LoI and the FTDR, the issue of radiation damage of both the fibres and SiPMs for their readout was discussed as having a negative impact on the possible performance of a CT/FT detector. This is the main focus of the rest of this document. We report on the results of current research from several LHCb groups, as well as a study of literature from previous experiments' work. Section 2 of this document will outline the foreseen parameters of the FT with Section 2.2 describing the radiation environment expected from FLUKA simulations. Results of research on the radiation hardness of the scintillating fibres and silicon photomultipliers are presented in Sections 3 and 4, respectively. An effort has also been made to study the fibre and SiPMs in irradiated prototype fibre-array modules, similar to those used by RWTH-Aachen for the PEBS experiment [3]. Section 5 discusses the Front-End Electronics. Section 6 briefly describes the performance expectation of the FT based on current results. Section 7 describes some of the aspects of engineering the FT as well as ensuring quality control. In the end, we hope to reach a conclusion determining the viability of a scintillating fibre and silicon photomultiplier readout system for the LHCb upgrade scenario.

2 Requirements on the SciFi detector

The tracking stations downstream of the LHCb magnet allow the measurement of charged-particle momenta by combination with the measurements made in tracking stations located before the magnet (VELO and TT). The required detector performance include a high hit efficiency, resolution in the bending plane at the level of 60–100 μm, a low budget material in the acceptance, and a readout electronics that allows 40MHz sampling. In addition, the detector must be able to operate over the full lifetime of the LHCb upgrade, and be resistant to the radiations after collecting $50\,\text{fb}^{-1}$.

We present in Section 2.1 the main requirements on the detector performance, and in Section 2.2 the expected radiations in the various regions of the detector.

2.1 Requirements on the detector performance

The main design requirements on the detector performance are the following:

- The hit detection efficiency must be in the vicinity of 99% in order to allow for efficient tracking, while keeping a low level of noise (2 MHz per 128 channels, as will be shown later). The acceptable noise rate is to be determined from simulation.

- The spatial hit resolution must be at the level of 60–100 μm. Better resolution is not necessary, as extrapolation of multiple scattering effects in the TT would dominate.

- The amount of material in the acceptance region should be kept to a minimum. As a baseline, the number of radiation lengths of the Silicon sensors in the current IT Silicon detector can be used as reference.
- The LHCb upgrade detector will be read out at 40MHz. The detector readout electronics must therefore be able to operate at this frequency, and the recovery time of readout channels should be short to reduce inefficiencies.
- Finally, the above requirements on performance must be fullfiled after the detector has been exposed to the radiations due to an integrated luminosity of $50\,\mathrm{fb}^{-1}$, with the option to replace the most degraded fibre modules.

2.2 The radiation environment of the SciFi tracker

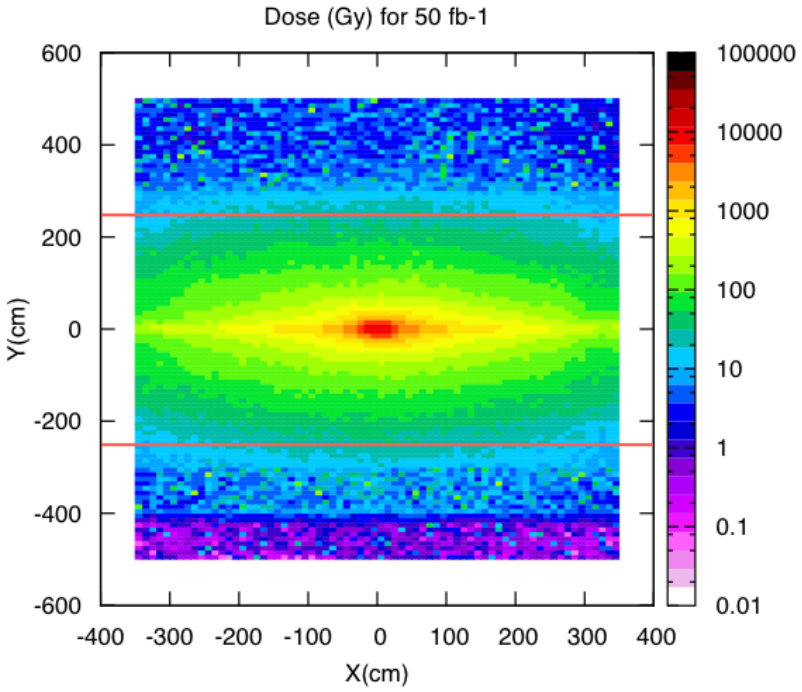

Figure 2: Mapping for the absorbed dose at $z = 783\,\mathrm{cm}$ using a cartesian grid. The results are expressed in Gy and correspond to an integrated luminosity of $50\,\mathrm{fb}^{-1}$. The two red lines are placed at ± 2.5m to indicate where the SiPM would be located.

This section presents the estimates for the radiation levels in terms of doses and 1 MeV neutron-equivalent fluence at the tracker station T1, located at $z = 780$ cm from the LHCb interaction point. The simulation and results presented in this note have been obtained using FLUKA [4], Flair [5] and SimpleGeo [6]. A detailed report of these studies can be found in Ref. [7].

The geometry is based on a previous description of the FLUKA LHCb geometry modeled by Lev Shektman [8] that was modified in order to obtain a more realistic and reliable geometry. The regions that were re-modeled to resemble reality more closely are the upstream of the interaction point, the VELO vacuum vessel and the Hadron calorimeter. Simulations were performed under upgrade conditions at $\sqrt{s} = 14$ TeV with the most recent magnetic field maps.

The dose and the 1 MeV neutron-equivalent fluence are estimated recording the energy deposited and the track-length fluence of particles, respectively, in a virtually superimposed cartesian grid. The grid is situated at $z = 783\,\text{cm}$ and extends from $-350\,\text{cm}$ to $350\,\text{cm}$ on the x axis and from $-500\,\text{cm}$ to $500\,\text{cm}$ in y and there are 70 bins in x, 100 bins in y and only one bin of 0.7 mm in z. The absorbed dose for an integrated luminosity of $50\,\text{fb}^{-1}$ obtained using this grid is shown in Fig. 2 with the corresponding projection on the $y-$axis in the $x[0, 10]$ slice shown in blue in Fig. 3.

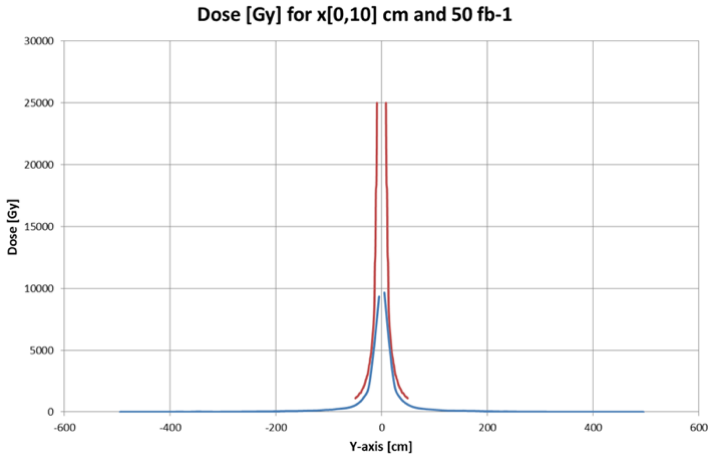

Figure 3: $1-$D projection of the Dose on the $y-$axis of Fig. 2 for $x[0, 10]\,\text{cm}$, shown in blue. The curve in red shows the result obtained using cylindrical rings that increase by 1 cm steps in their radius up to 50 cm. The results correspond to an integrated luminosity of $50\,\text{fb}^{-1}$.

Also, the dose deposited was recorded in cylindrical rings increasing by 1 cm steps in their radius around the beam pipe extending from 8 cm out to 50 cm to obtain a more accurate result for the inner region. The 1D projection for the result obtained is shown in red in Fig. 3. From this figure one can see that the radiation field is very peaked near the beam pipe and falls by a factor of more than 20 to marginal levels (with regards to fibre damage) within 50 cm.

An additional simulation with a larger number of initial collisions ($\approx 10^6$) is performed to study in more detail the region with high dose near the beam pipe. For this study a grid of 40cm per 40cm in x and y and 0.7 mm in z is defined at $z = 783\,\text{cm}$, using 1 cm binning in x and y. The result is shown in Fig. 4 for an integrated luminosity of $50\,\text{fb}^{-1}$.

The 1 MeV neutron-equivalent fluence is computed using the grid with the same

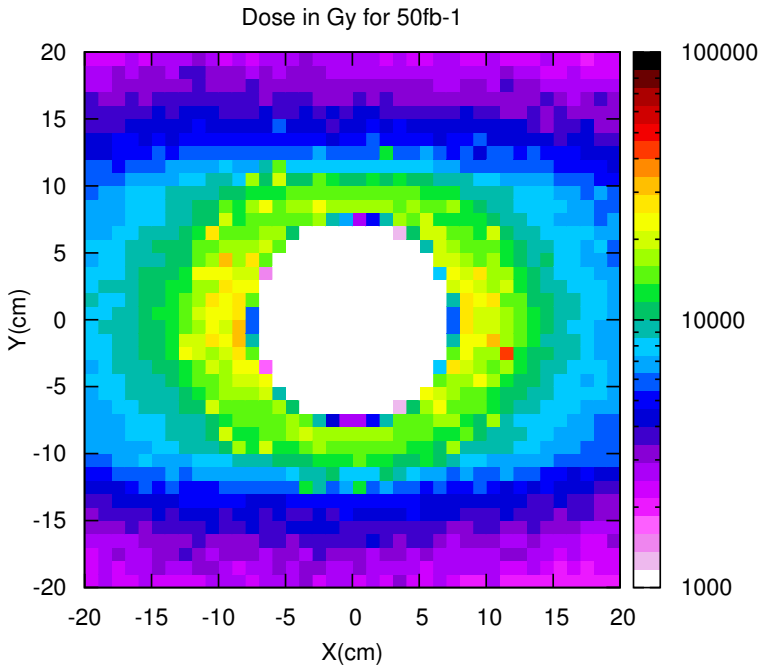

Figure 4: Mapping for the absorbed dose at $z = 783$ cm using a cartesian grid. The results are expressed in Gy and for an integrated luminosity of $50\,\mathrm{fb}^{-1}$. One million primary collisions were used for the simulation. A grid of 40 cm per 40 cm in x and y and 0.7 mm in z is used.

binning as for the dose. The result obtained per collision is shown in Fig. 5 with the corresponding projection on the $y-$axis in the $x[0, 10]$ slice shown with a logarithmic scale in Fig. 6, from which we determine the radiation dose of $6 \cdot 10^{11} n_{\mathrm{eqv}}/\,\mathrm{cm}^2$ at the position of the SiPMs (± 250 cm).

The FLUKA simulation indicates that for a cross section of 72 mb and a luminosity of $50\,\mathrm{fb}^{-1}$ at a position of 8 cm approximately from the beam axis, the peak dose in the fibres is of the order of 26 kGy and an average dose integrated over the first two rings gives 23 kGy, both with a statistical error of 10%.

Notice that the magnetic field created by the LHCb dipole is responsible for the horizontal widening of the distribution of dose as seen in Fig. 2. This happens in all regions downstream of the dipole.

Ref. [7] presents a detailed study of a shielding made of 95% of Polyethylene and 5% of Boron on the neutron fluence. The neutron fluence in the SiPM and electronics region is found to be reduced by a factor two or more with a 10 cm-thick shield. The design with shielding is taken as baseline for the SiPM radiation studies presented in this document.

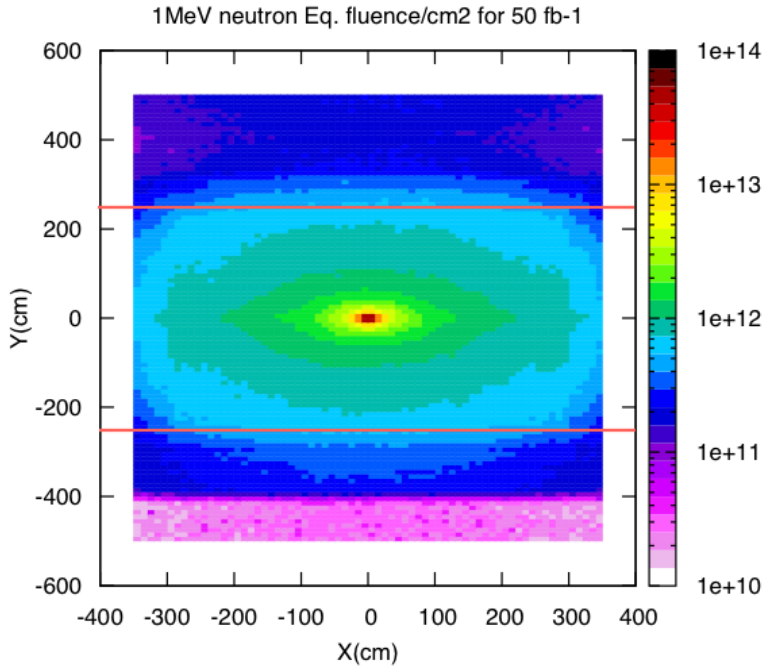

Figure 5: Mapping for the 1 MeV neutron-equivalent fluence at $z = 783\,\text{cm}$ using a cartesian grid for an integrated luminosity of $50\,\text{fb}^{-1}$. The two red lines are placed at $\pm$2.5m to indicate where the SiPM would be situated.

3 The Scintillating Fibre

Scintillating plastic fibres are considered as the active detector elements for the SciFi upgrade project. For the time being, all experimental work has been concentrated on the multi-clad blue emitting fibre of type SCSF-78MJ from Kuraray. It is currently considered as the baseline fibre due to previous experience and knowledge using scintillating fibres in other experiments. The question of a possible alternative fibre is briefly addressed in Sec. 3.2. Discussions with colleagues from Aachen (S. Schael et al., RWTH Aachen, Germany) have indicated that it will take nearly two years to acquire the amount of fibre needed for production of the Fibre Tracker given current module production loss inefficiencies.

3.1 Properties

We intend to use plastic scintillating fibre with a circular cross section having a diameter of 250 μm, including two cladding layers of nominally 3% total thickness each. The core of the fibre is doped polystyrene with two outer claddings of decreasing indices of refraction. The inner cladding is made of polymethylmethacrylate (PMMA) and the outer cladding made of fluorinated-PMMA. The trapping efficiency for isotropically emitted (scintillation)

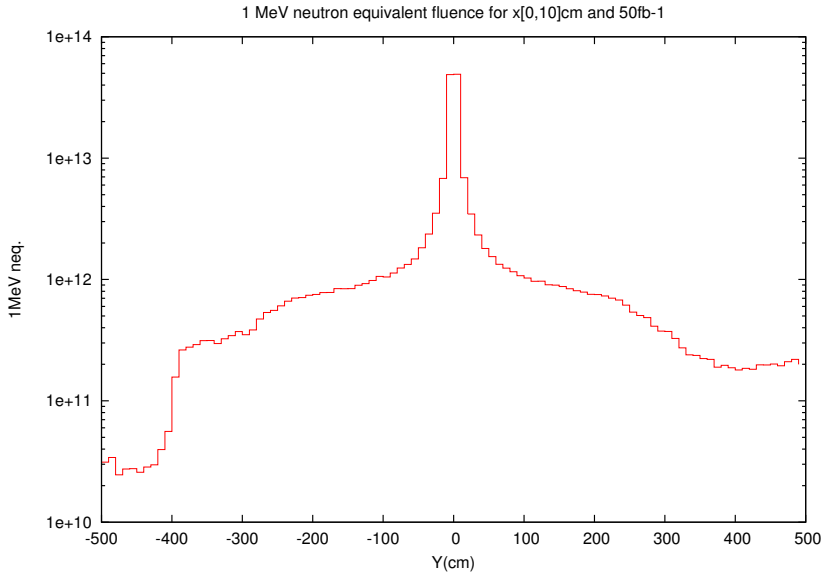

Figure 6: $1-$D projection of the 1 MeV neutron-equivalent fluence per cm^2 on the $y-$axis of Fig. 5 for $x[0, 10]$ cm, using logarithmic scale.

light in one hemisphere is at least 5.34% (helical paths or non-meridional light rays will increase this but these photons are usually rapidly absorbed) and the numerical aperture of the fibre is 0.72. The nominal emission spectrum (for emission very near to the detection point) for the SCSF-78MJ fibre extends from about 400 to 600 nm and peaks at 450 nm, as seen in Fig. 7, with a bulk optical absorption length of >3.5 m.

Typically, there is a short and long component to the attenuation length, due to geometrical effects in the fibre, as well as a strong wavelength dependence on the absorption length due to reabsorption of the shorter blue wavelengths by the scintillation dyes and some discrete higher wavelengths by the polystyrene, as seen in Fig. 8. The effect on the emission spectrum and the optical absorption length by radiation will be further addressed in Sec. 3.3.

The decay time of the scintillation light is nominally 2.8 ns and the light yield is expected to be around 8000 photons/MeV[1] or 1600 photons per mm of scintillating fibre. The various efficiencies related to transport and detection of the photons lead a reduction of the yield by typically two orders of magnitude.

Typically, for a minimum ionizing particle (MIP), one observes between 15 and 20 photoelectrons per mm of scintillating fibre near the source as seen by a SiPM. This light yield and timing is sufficient for the needs of the scintillating fibre tracker.

The investigated fibre is of the S-type (the polystyrene chains in the fibre core are aligned along the fibre axis) which gives the fibre a higher strength against cracking. However, the attenuation length is typically 10% shorter for S-type compared to the Non-S-type, according to the manufacturer. The minimum bending radius, recommended

[1]Kuraray does not specify this number but it is compatible with the findings of previous experiments [9].

by Kuraray, for this fibre type, is about 12.5 mm.

The fibres will be bonded into ribbons consisting of five staggered fibre layers with a pitch of half the fibre diameter, and a total length of 2.5 m. The fibres will be covered with a thin, clear epoxy layer (Epotek 301-2) during ribbon production, and yet again during final ribbon molding. A small percentage of titanium-dioxide will be added to the epoxy to reduce channel cross-talk. Readout will be by SiPM arrays on one fibre end only. The other end may be equipped with a reflecting mirror to increase light yield at the readout end. Signal timing as well as light yield gain will determine this.

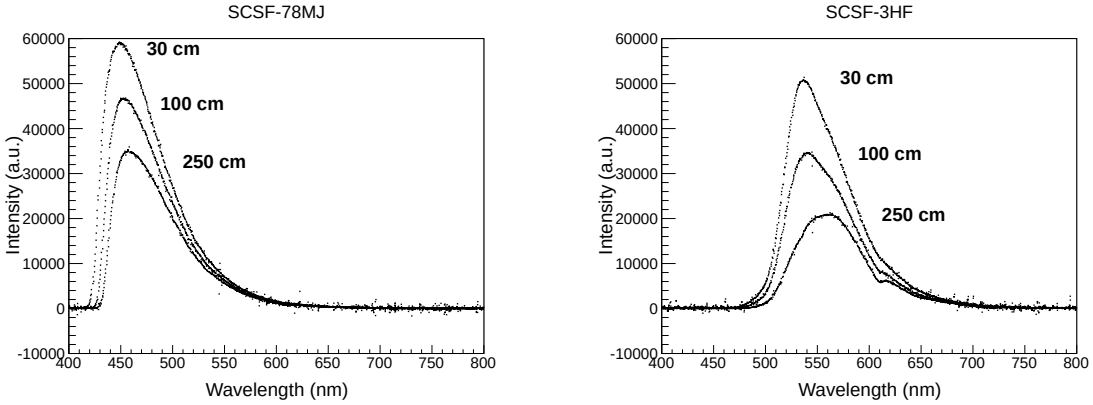

Figure 7: The wavelength spectra observed in 1 mm round Kuraray SCSF-78MJ (left) and SCSF-3HF (right) scintillating fibres. A 370 nm LED was used to stimulate the fibre and was read out with an intensity calibrated Hamamatsu C10083CA-2050 photospectrometer.

3.2 Possible alternative fibres

Large volumes of scintillating plastic fibres are produced by only two companies: Kuraray Co. LTD., Japan, and Saint-Gobain Crystals (formerly Bicron), USA. Both producers offer blue and green emitting fibres with nominally very comparable properties. Experiences from previous experiments in Ref. [10–12] have revealed the better quality of Kuraray fibre. Its light absorption length is significantly longer, and perhaps even more important for a high resolution tracker, the geometrical parameters like roundness, tolerance of the core diameter and cladding thickness are much better controlled than for comparable Saint-Gobain fibres.

A potential alternative to our baseline fibre is the green-emitting fibres with 3-Hydroxyflavone (3HF) as wavelength shifter which both suppliers advertise as more radiation hard than other formulations. Kuraray and Saint-Gobain both market the SCSF-3HF(1500) (1500 ppm). The emission spectrum, for non-irradiated short fibres, peaks at about 530 nm and extends to about 650 nm, as seen in Fig. 7. The large Stokes shift leads to a somewhat longer absorption length than for blue emitting fibres. As radiation damage is known to affect primarily the optical transmission of the fibre core

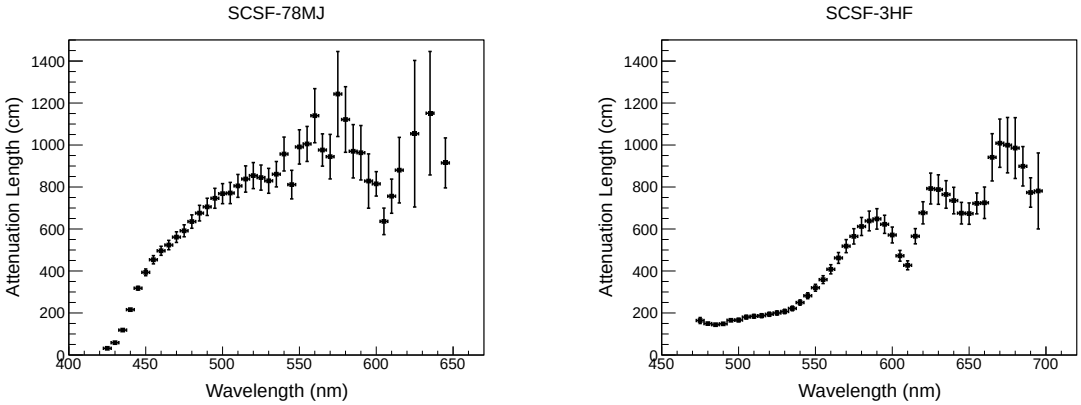

Figure 8: The attenuation of discrete wavelengths seen in 1 mm round Kuraray SCSF-78MJ (left) and SCSF-3HF (right) scintillating fibres. The attenuation length is found from a single exponential fit of the measured intensities along positions from 50 cm to 270 cm. A 370 nm LED was used to stimulate the fibre and was read out with an intensity calibrated Hamamatsu C10083CA-2050 photospectrometer.

at shorter wavelengths (< 500 nm) [11, 13], the 3HF fibre is potentially more radiation hard than blue types. Hara et al. [14] have previously studied irradiated 3Hf fibres and express the measured damage in terms of the ratio of the irradiated and initial attenuation lengths, where $\lambda/\lambda_0 = \alpha + \beta \cdot log_{10} D([\text{kGy}])$ and with the parameters found in irradiations with a Co-60 source up to 7 kGy, $\alpha = 0.512$ and $\beta = -0.144$. For a dose of 23 kGy, the maximum dose received by fibres near the LHCb beam pipe, this leads to an expected damage of $\lambda/\lambda_0 = 0.31$.

Unfortunately, the 3HF complex alone has a relatively low quantum efficiency and its absorption spectrum overlaps poorly with the emission of polystyrene by itself. Usually a 1% component of p-terphenyl is added as primary fluor, however the light yield remains well below the one of blue emitting fibres (L. Archambault et al. [15]) found a 45% difference). Reading out 3HF fibres with the blue-optimized SiPM detectors from Hamamatsu or KETEK available today would lead to a further yield reduction of about 30%. Development of SiPMs with high green sensitivity is underway (KETEK and Hamamatsu), however, and would negate this problem.

A significant problem with the 3HF fibre is the long decay time constant of 7 ns. For the proposed SciFi tracker upgrade, this is a substantial disadvantage. Including the 15 ns propagation time of the signal from the furthest positions, it significantly complicates the task of collecting the signal within a single bunch crossing interval. Addition of a mirror to the fibre end further complicates the timing of the signal. Saint-Gobain has a fast, green (492 nm) scintillating fibre, the BCF-20, but the fluors were found to be damaged quite easily under irradiation and cannot be considered.

In conclusion, the 3HF fibre by Kuraray is, for the time being, the only potential alternative to the baseline fibre. We keep our interest in this fibre and intend to include

it in some of the future studies. In the unlikely case the baseline fibre fails to prove full viability of the SciFi concept, we will intensify our experimental activities on the 3HF fibre.

3.3 Radiation Tolerance of the Fibre

In the inner-most region of the detector, at about 8 cm from the beam pipe axis, the scintillating fibres would be exposed to an accumulated radiation dose of approximately 23 kGy (see Sec. 2.2). The expected dose drops rapidly, both in the horizontal and vertical directions, and becomes expectedly marginal (<1 kGy) at distances of about 50 cm [7]. Radiation damage to plastic fibres has been systematically investigated in the early 1990s [13] and the optical changes to the base material were identified as main cause for the degradation of their light output. Radiation damage leads to a reduction of the optical absorption length and the viability of a fibre at a given radiation load depends crucially on its length. However, also the basic scintillation and wavelength shifting mechanisms (fluors) as well as other additives can suffer damage and contribute to the performance degradation. From the beginning, the impact of radiation dose rate, radiation type and environmental effects (presence of oxygen) as well as recovery effects were controversially discussed in the literature. Analysis of the publications of a number of irradiation experiments which have been performed for our baseline fibre or similar polystyrene based blue emitting fibres revealed results which partly disagree and the conclusions which are vague or even in full contradiction [16].

3.3.1 Irradiation experiments

The need for dedicated radiation tests was recognized at the very beginning of the SciFi study. Given the unsatisfactory result of the literature study, it was considered mandatory to perform a series of radiation experiments with the SciFi baseline fibre in a configuration which comes close to the one in the final detector. While some of the experiments are completed, further complementary tests are currently under way or will be performed in 2013.

We describe first a set of exploratory irradiation tests which were launched at the early stage of the SciFi project exploiting the available fibre samples and facilities. These tests have not led to fully conclusive results. We concentrate then on a recent irradiation experiment at the CERN PS facility which resulted in quantitative conclusions.

The Dortmund group irradiated several bundles of fibres with protons of 24 MeV energy to doses of up to 100 kGy. A significant degradation of the optical transparency was observed for the highest dose, however the small length of the irradiated zone and the absence of control measurements on non-irradiated samples prevented the extraction of quantitative results.

The same group is currently performing in-situ irradiations in the LHCb cavern on three sets of 1.1 m long fibres. The samples were installed in 2012 during TS1 on the shielding wall close to the VELO. The expected doses are in the sub-kGy range. Measurements of

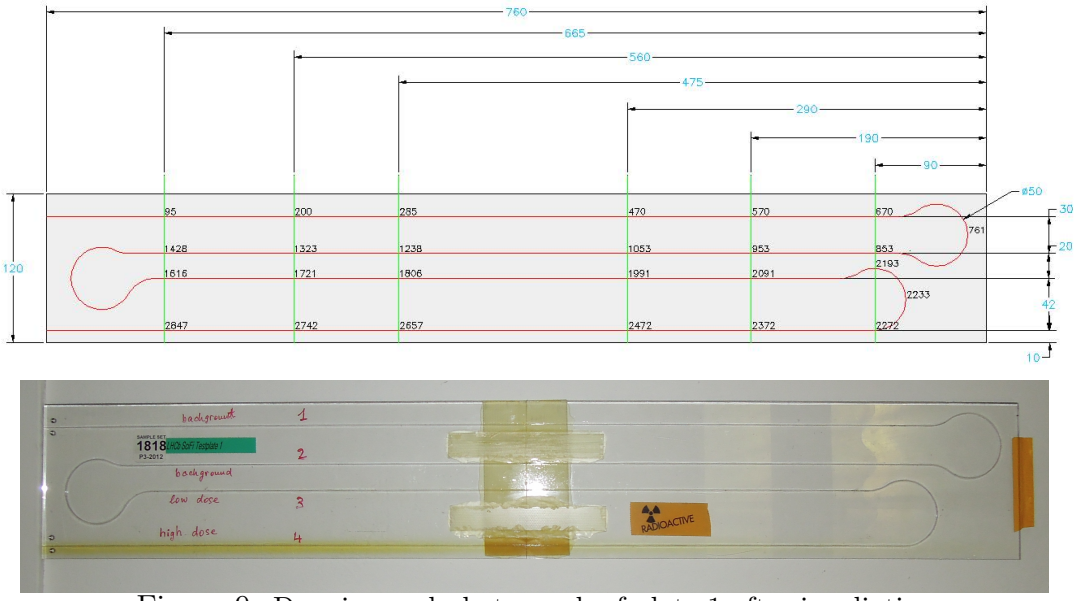

Figure 9: Drawing and photograph of plate 1 after irradiation.

the relative light yield as a function of the position of a Sr-90 source were performed during TS2 and TS3. The measurements and the analysis suffer from a number of limitations inherent to the in-situ set-up and the availability of only two data points (TS2, TS3). More data is expected from the Christmas 2012 stop and after the 2013 proton-ion run. The relatively low dose levels makes it however difficult to derive a conclusive result.

The Heidelberg group parasitically used an irradiation campaign of FPGAs at the MPI Heidelberg to irradiate fibres with 22 MeV protons. The limited dose of approximately 1.5–2.5 kGy and the short length of 4 cm which was exposed to the beam didn't allow to observe a clear effect. Future tests at the Karlsruhe irradiation facility at multiple higher doses and longer fibre sections are planned for February 2013.

In November 2012, a radiation test was performed at the CERN PS with 24 GeV/c protons on a test plate which contains 8 SCSF-78 fibres of 2.94 m length. Details of this test and the performed characterization measurements can be found in [17]. A second identical plate was kept non-irradiated as reference. The samples consist of a plexiglass plate with a grove in which 8 fibres, arranged in 4 layers of 2 fibres each, are placed together with a thin layer of epoxy glue of type EPOTEK 301-2FL (see Fig. 9). To accommodate the total fibre length of $L = 2942$ mm on the plates, the fibres are arranged as 4 legs (of approx. 75 cm length) with 3 turn points (TP). The bending radius at the turn points is 25 mm and hence a factor 2 larger than the recommended minimum radius. The glue was unloaded, i.e. no TiO_2 powder or other substances were admixed to it. The two ends of the fibre set reach the edge of the plate and, after polymerization of the glue, they were machined to optical quality by means of a diamond tool on a milling machine. One end serves as port to connect a photodetector or spectrometer. The other end of the fibre allows to investigate the effect of a reflecting mirror on the fibre characteristics.

Plate 1 was irradiated with protons of 24 GeV/c in the T7 area of the CERN PS

irradiation facility. Protons from the primary PS beam form a horizontal beam of about 1×1 cm^2 in size. The plate was aligned with the beam axis and tilted by 10 mrad w.r.t. the horizontal plane. In this configuration the beam spot was expected to cover the full length of the plate (76 cm). The plate was mounted on a motorized XYZ table which allowed changing the positioning during the irradiation. The irradiation was programmed to take place in two steps: in a first period lasting 4.5 hours, leg 4 (far end) was irradiated to a total proton fluence of $7.1 \cdot 10^{13}$ p/cm^2 (equivalent to 22 kGy) followed by a second step lasting 8 minutes, in which leg 3 was exposed to protons up to a total fluence of $9.5 \cdot 10^{12}$ p/cm^2 (equivalent to 3 kGy). The relative uncertainty is 10% for both values. Legs 1 and 2 were expected to receive only background radiation from neutrons. This resulted in a neutron fluence of about $5 \cdot 10^{12}$ n/cm$^2 \pm 20\%$ which represents a negligible ionization dose. The actually received radiation doses and fluencies were extracted from the forward currents of a set of four PIN diodes and the activation of aluminium foils which were attached to the plate right above the fibre locations. From the discolouring of the plexiglass plate, visible in the region of leg 4, it appears that the irradiation was uniform over only about 70% of the plate's length. In accordance with the rules in place at CERN, the plate could be extracted from the irradiation zone after a cool down time of 7 days.

3.4 Results

A number of measurements were performed on the irradiated plate and for reference also on the non-irradiated one. In all measurements, the coupling between the fibres and the photodetectors was performed without optical grease. Due to time constraints, only the optical absorption length could be measured for plate 1 prior to the irradiation.

3.4.1 The optical absorption length

The fibre samples were excited by UV light from a LED (wavelength = 385 nm, beam spot size = 3 mm) which was mounted directly above the test plate. The LED excites the second fluor of the fibre, i.e. the fibre will respond with its normal emission spectrum. The light output is measured by means of a calibrated ($\pm 2\%$) UV-enhanced photodiode of type Newport 818-UV of 10 mm active diameter. Its photocurrent is measured as a function of the distance of the excitation point from the end where the photodetector is placed. Despite manual positioning of the LED, the method proved to be reproducible the the level of $<5\%$. The data for plate 1 before and after irradiation are shown in Figs 10 and 11. The bulk absorption length is typically extracted from a single exponential fit to the data, $I(d) = I_0 exp(-d/\lambda_{abs})$, for positions greater then 50 cm. A double exponential fit is needed to account for the short attenuation component less than 50 cm owing to geometrical path effects in the fibre. More complex parametrizations are needed when including the mirror at the far end. A wavelength dependence on attenuation length is also oberved, as seen in Fig. 7, such that the bulk attenuation length also depends on the quantum efficiency of the photodetector over the wavelength spectrum.

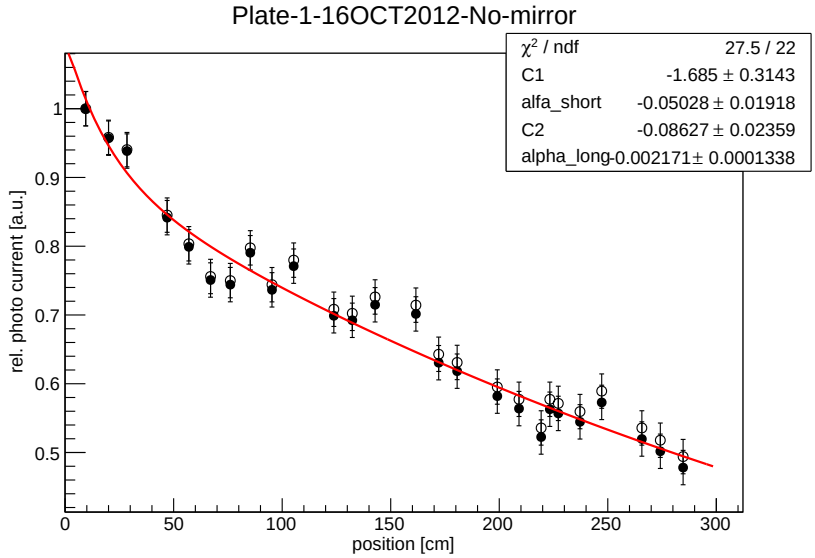

Figure 10: Relative light yield as function of the excitation distance for plate 1 before irradiation. Open symbols: As measured with the PIN diode. Full symbols: Scaled to the spectral response of a KETEK SiPM detector.

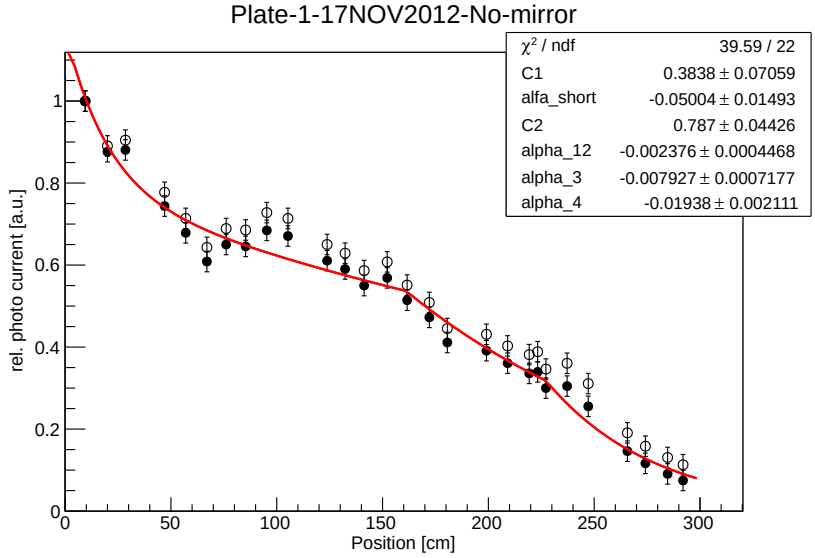

Figure 11: Relative light yield as function of the excitation distance for plate 1 after irradiation. The open and filled symbols were used as in the Fig. fig:UV-Pre-Irrad. The scaling effect reaches almost 30% at the farthest distance.

The light yield and the absorption lengths measured in this way correspond to the averages over the fibres' emission spectra weighted with the quantum efficiency of the photodiode. The latter varies in a rather linear way from 50% at 400 nm to 80% at 600 nm. The photon detection efficiency (PDE) of the KETEK SiPM detector (see Sec. 4.2) which was used for the measurements with the Sr-90 source, described below, and which is a

Table 1: Optical absorption length before and after irradiation. All values are in cm. The data for legs 1 and 2 include the long/short absorption length, 3 and 4 only contain the long component. The errors are statistical only.

leg	plate 1 non-irrad.	plate 1 irrad.	plate 2
1 and 2 (0 kGy)	439^{+28}_{-25} / 20^{+8}_{-5}	422^{+97}_{-66} / 20^{+8}_{-5}	346^{+13}_{-12} / 10^{+40}_{-5}
3 (3 kGy)	439^{+28}_{-25}	126^{+13}_{-10}	346^{+13}_{-12}
4 (22 kGy)	439^{+28}_{-25}	52^{+6}_{-5}	346^{+13}_{-12}

candidate to be used in the SciFi detector, shows a very different spectral form. It peaks at about 425 nm, drops by 15% at 400 nm and by 50% at 550 nm. The knowledge of the fibre's emission spectra, before and after irradiation, for different excitation distances, allows taking into account the different spectral responses of the photodetectors.

The measurements after irradiation are described by a combination of exponentials, where the individual segments of the fit were defined such that they coincide at the turn point positions of the plate. The fits resulted in the absorption lengths summarized in Table 1. The long and short components of the absorption length are shown. The short absorption length describes the rapid light absorption of helical light rays and/or possible 'cladding' light along with wavelength reabsorption (in the far blue).

3.4.2 Emission spectra

The emission spectrum of the fibres was measured by means of an Ocean Optics spectrometer (type SD2000, CCD based, 2048 channels, sensitive range 200–900 nm). The fibres were again excited by the the UV-LED. The wavelength dependent response of the spectrometer was calibrated in order to obtain true emission spectra (details can be found in [17]). Figs 12 and 13 show the emission spectra of the non-irradiated and irradiated samples for excitation at different positions. The light had to propagate between 10 and 280 cm from the excitation point to the end where the spectrometer was coupled. At 10 cm the spectra are identical and peak at 450 nm. The absorption and shift of the spectrum towards longer wavelength increases with the length of the light path. This effect is much more expressed for the irradiated fibre, where the average emission wavelength becomes about 530 nm for excitation at about 280 cm from the spectrometer end.

A spectrum was recorded, where the fibre was excited in the highly irradiated zone at 280 cm from the readout end. The fibre was however read out at the other end, i.e. the light had to propagate only 14 cm to the spectrometer. The recorded spectrum had the identical shape as a spectrum taken at 10 cm in the standard readout configuration. The modification of the observed emission spectrum is therefore entirely due to the enhancement of the optical absorption particularly in the blue wavelength region.

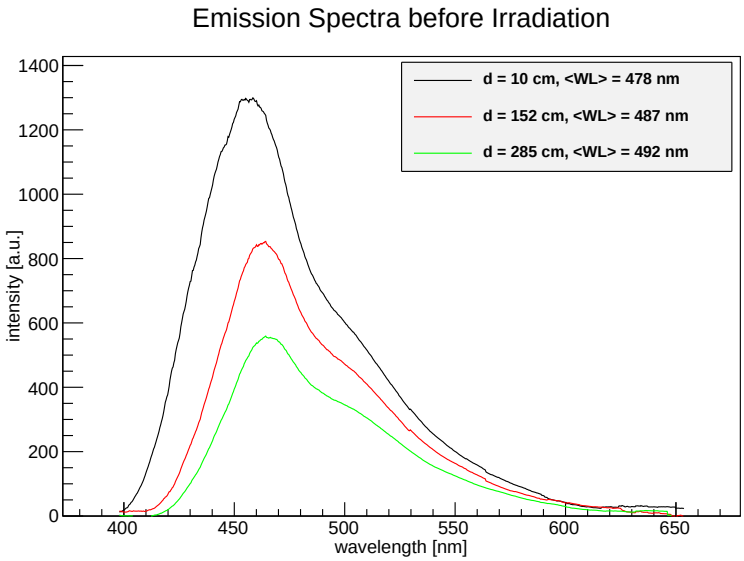

Figure 12: Emission spectra, as observed at the fibre end, before irradiation for different excitation points.

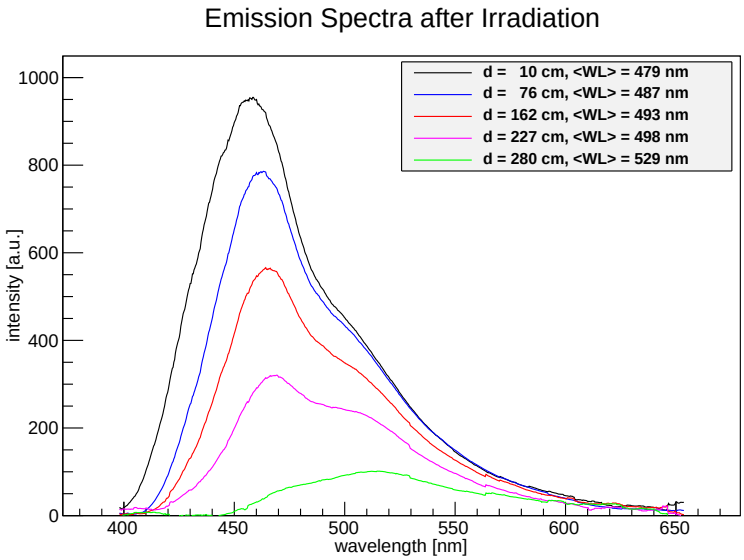

Figure 13: Emission spectra, as observed at the fibre end, after irradiation for different excitation points.

3.4.3 Measurement with ionizing particles

The samples were exposed to a Sr-90 source which is integrated in a simple electron spectrometer, in the following called e-gun. A set of Tungsten collimators combined with a magnetic solenoidal field permit to select electrons of 1-2 MeV energy which can be considered as minimum ionizing particles (MIP). The range of such electrons is between 0.5 and 1 cm in plastic. Two aligned scintillating fibres of 1 mm diameter, mounted behind

the exit slit of the e-gun and read jointly by two SiPM detectors at either side, served for triggering. The measurements with MIPs were performed with a SiPM from KETEK of 1×1 mm^2 size centred on the polished fibre ends. It has a pixel size of 50 μm and provides a gain of 10^6 at an overvoltage of 3 V. The SiPM signals were amplified (current amplifier, bandwidth 500 MHz, gain 15) and read out by a digital oscilloscope which integrated the pulse shapes (equivalent to a charge measurement) and histogrammed the results. The acquisition was triggered by a coincidence of the above mentioned trigger fibres with the signal from the fibres under test. For the latter a threshold of about 0.5 p.e. was set. The geometrical configuration and the inclusion of dark noise in the spectra makes the analysis of the these measurements less straight forward than the optical measurements discussed previously. The precision of the results is estimated to be in the ±10-20% range.

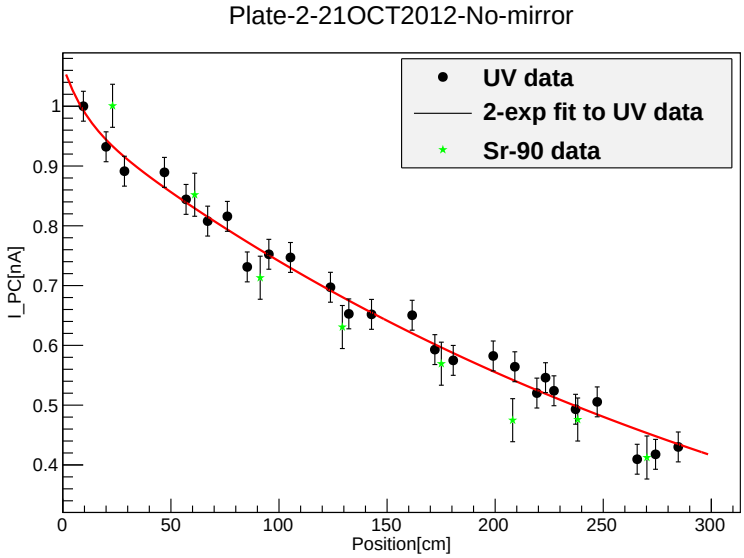

Figure 14: Plate 2, non-irradiated: Relative light yields following UV excitation and exposure to electrons from the Sr-90 source.

The Sr-90 data, compiled in Figs 14 and 15 shows a very similar dependence on the excitation distance as the UV-LED data (after scaling the latter to the spectral response of the SiPM). It therefore appears that both the scintillation and wavelength shifting mechanism of the fibre are – if at all – only marginally affected by the applied radiation levels, and that the main performance degradation of the fibre can be solely explained by the loss of its optical transparency.

3.4.4 Effect of a reflective mirror at the fibre end

The yield increase due to a reflective mirror was investigated both for UV-LED and Sr-90 excitation. The mirror consisted of a glass substrate with a thin Aluminium layer plus a protective MgF_2 coating. The reflectivity in the blue to green range of the spectrum is typically around 90%. The mirror was held mechanically against the polished fibre ends. No optical coupling medium was used, i.e. a loss due to Fresnel reflections of the order

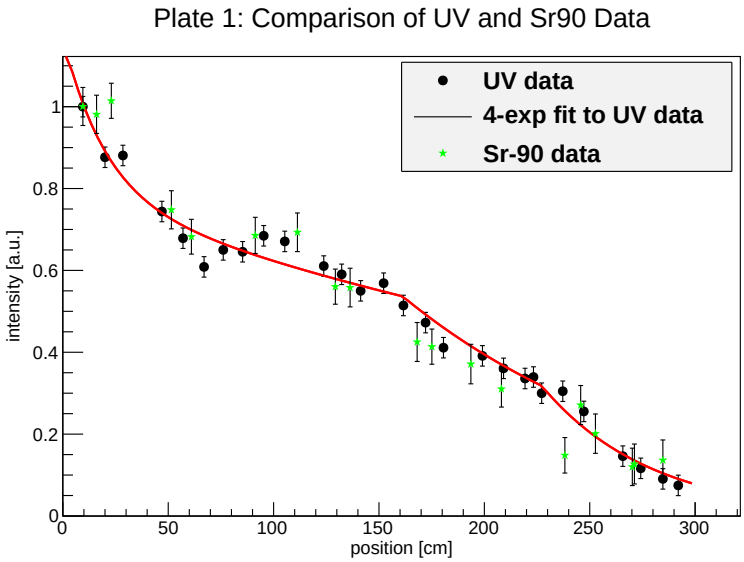

Figure 15: Plate 1, after irradiation: Relative light yields following UV excitation and exposure to electrons from the Sr-90 source.

of 10% can be expected. The effect of the mirror is demonstrated in Fig. 16 for plate 1 prior to irradiation. The gain is largest close to the mirror and reaches about 70-80% while it is about 20% on the first meter from the photo detector. After irradiation, the same maximum gain close to the mirror is found, however the gain drops within 50 cm from the mirror to a level of about 10%. The mirror potentially doubles the propagation time of the light from 15 to about 30 ns which would exceed the LHC bunch crossing interval [18]. We assume that a timing cut applied on the level of the front-end will avoid signal spill-over and consequently limit the gain by the mirror to the far region (seen from the photodetector).

3.5 Discussion and conclusions

The irradiation of the Kuraray SCSF-78 fibre to fluences of up to $7.1 \cdot 10^{13}$ p/cm^2 (equivalent to 22 kGy) leads to a significant reduction of the optical absorption length. The primary scintillation and wavelength shifting mechanisms appear to be unaffected. On a time scale of 2 months, the measured absorption lengths are stable and no annealing effects were observed. Annealing is generally attributed to the oxidation of free radicals produced during the radiation exposure [19]. The fact that our fibres are embedded in epoxy glue, which may act as a barrier for oxygen, is possibly suppressing a recovery of the optical transmission. It should be noted that a possible fast annealing component during the first 7 days after the irradiation would have remained undetected. The available data limits the time constant of such a component to about 3 days.

The measured damage, expressed as $K = \lambda_{abs}/\lambda_{abs,0}$, was fitted to a model proposed by Hara et al. [14]: $K = \alpha + \beta \cdot log_{10}(D)$, with D being the dose in kGy. The fit yielded the parameters $\alpha = 0.381$ and $\beta = -0.196$ (see Fig. 17). The model appears to describe the

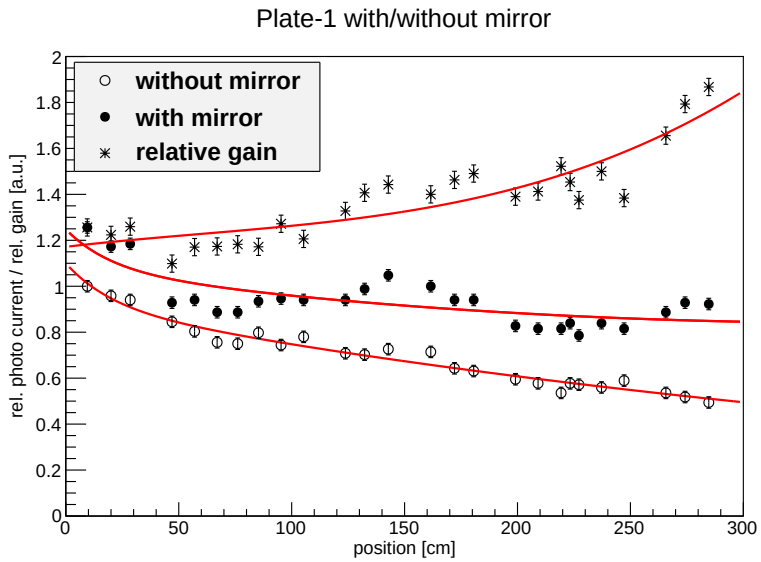

Figure 16: Plate 1, before irradiation: Relative light yields following UV excitation with (filled) and without (empty symbols) mirror. The stars show the relative gain due to the mirror.

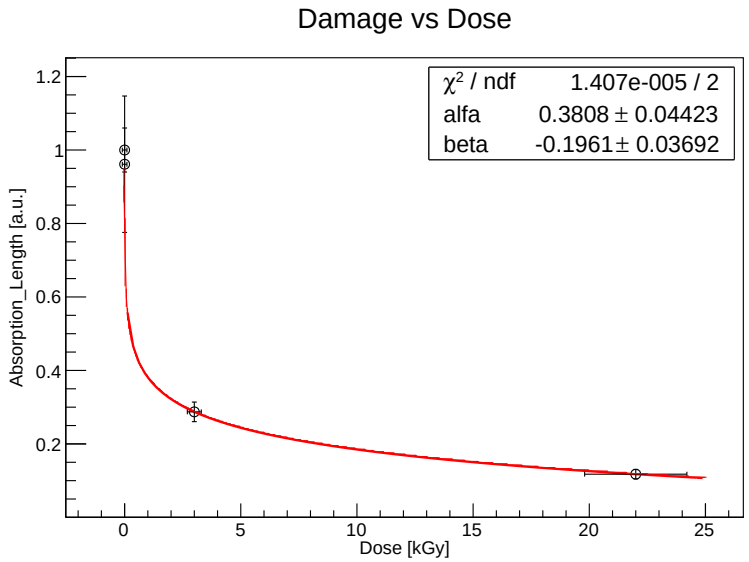

Figure 17: Damage versus dose. The data are fitted by the model of Hara et al.. The points corresponding to before irradiation and legs 1 and 2 after irradiation (background) were associated with a dose of 1 Gy in order to include it in the logarithmic Hara model.

data very well. The data points corresponding to before irradiation (0 kGy) as well as legs 1 and 2 after irradiation (background = 0 kGy) are included in the plot. By construction, they cannot be fitted by the logarithmic Hara model, however the fit function goes nicely through these points, too. Comparing the magnitude of the parameters from Hara et al. for the 3HF fibre, where $\alpha = 0.512$ and $\beta = -0.144$, to the values measured here for the SCSF-78MJ fibre, the 3HF is relatively more radiation hard.

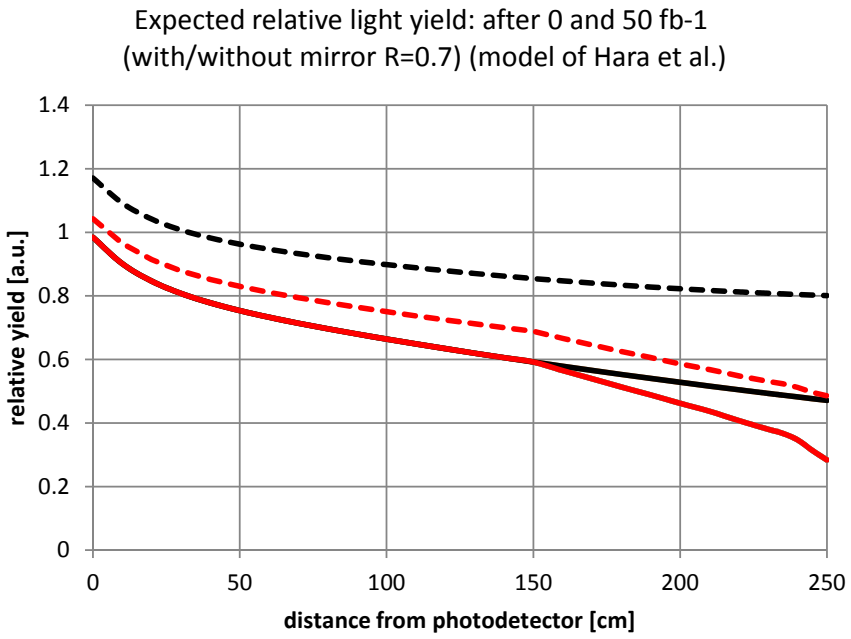

Figure 18: Prediction of the relative yield as a function of the excitation distance. The curves are for an non-irradiated fibre (black line) and for a fibre after irradiation to the equivalent of 50 fb^{-1} (red line). The dashed lines indicate the increased yield to the use of a mirror with a reflectivity of 70%.

With these parameters fixed and based on the input from the aforementioned FLUKA simulation, the model was then used to predict the variation of the optical absorption length along the fibres. The resulting corresponding relative light yields, with and without the use of a mirror, are shown in Fig. 18.

Thanks to the very peaked radiation profile expected at the position of the SciFi detector, a noticeable reduction of the absorption length is only expected for a circular region of about 1 m diameter around the beam pipe. Significant damage is even limited to a diameter of just 20 cm. In the innermost region, where the light yield is already reduced by the 'normal' absorption of the fibre to about 50%, the radiation damage will further decrease it to about 30%. The use of a mirror has clearly a beneficial effect on the light yield, particularly in the innermost region. The mirror increases the light yield of an irradiated fibre above the value of a non-irradiated fibre. The relative gain of a mirror is shown in Fig. 19.

3.6 Remaining work

In the coming months, more data is expected to arrive from the currently ongoing irradiation tests described in Sec. 3.3.1. Assuming the new data to confirm the above findings, it will strengthen and consolidate our experimental basis for a reliable viability assessment. In parallel we will regularly remeasure the irradiated samples and search for signs of annealing

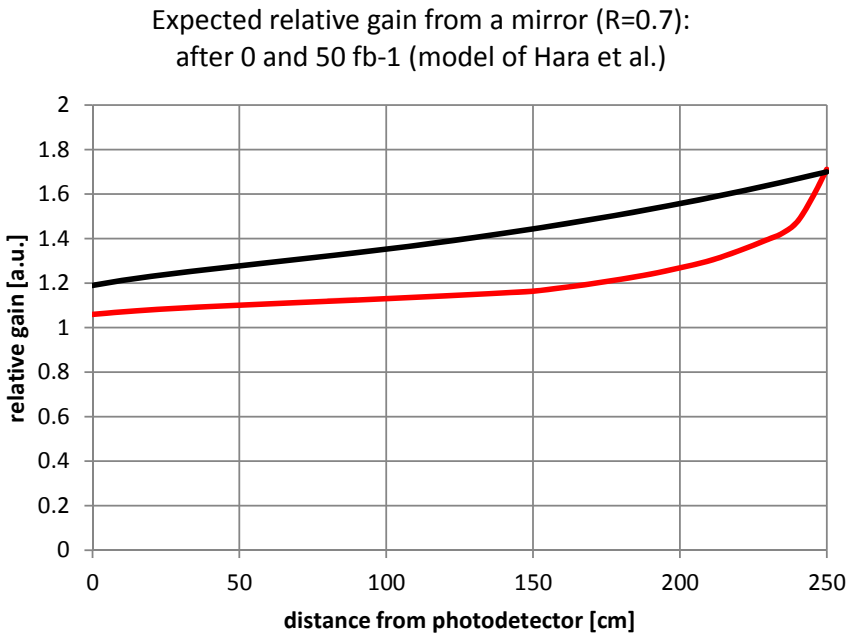

Figure 19: Prediction of the relative gain due to the use of a reflective mirror with 70% reflectivity for a non-irradiated (black line) and after 50 fb^{-1}.

effects. The irradiated sample is also an interesting testing ground for the evaluation of SiPM photodetectors, particularly after neutron irradiation.

The foreseen cold operation of the SiPM photodetectors (see Sec. 4), may lead to a reduced temperature of the fibre in the region close to the readout. The Aachen group (R. Greim, M. Wlochal, RWTH Aachen, private communication) successfully flew the Perdaix fibre tracker on a balloon experiment which exposed it to temperatures as low as -35°C. Despite this positive result, we intend to perform a number of systematic thermal tests, addressing the low temperature behaviour of the fibre itself as well as of glued fibre assemblies

4 The Silicon Photodetector

There are several challenging requirements to the detector which are discussed in this chapter. In particular, the SiPM detectors are known to suffer from neutron radiation. With Hamamatsu and KETEK we have two SiPM detector suppliers interested in the development of segmented multichannel SiPM arrays for the scintillation fibre tracker application. The pitch and dimensions of the detector are optimized to the available fibre of 250 μm and a possible stack-up of 5 layers of fibres. The pitch is 250 μm and the pixel size is about 55 μm.

In the first two sections of this chapter we describe tests done with Hamamatsu and KETEK detectors. The measurements of the noise cluster rate were made with

the VaTa64HDR16-V2R1 [20] chip and taking the recorded noise spectrum as input, a simulation was performed to obtain the results for a faster "LHCb-like" readout [2].

To suppress the noise while keeping a high detection efficiency, requires a detector with high photon detection efficiency (PDE), with low cross-talk (x-talk) between micro-pixels [3] and after-pulsing. KETEK has provided samples which have shown almost twice the PDE of current Hamamatsu detectors and improved x-talk performance. Hamamatsu will release structures with similar performance in 2013. Moreover operating the detector after neutron irradiation at the level of $D = 3 \cdot 10^{11} n_{\mathrm{eqv}} / \mathrm{cm}^2$ requires cooling down to about $-40°\mathrm{C}$ to allow sufficient noise suppression.

The geometrical loss of the detector is mainly due to gaps between adjacent detectors. In order to reduce dead regions, large continuous structures with at least 64 channels with a minimal gap between chips is a strong requirement. Hamamatsu has provided a package that fulfils all requirements.

4.1 Detector R&D with Hamamatsu

In 2009 Hamamatsu customized the first multichannel arrays, 32 channels with 250μm pitch for a fibre tracker application. The detectors were used for several fibre tracker prototypes and successfully used in a small balloon experiment during 2009 and 2010 [22]. The detectors were further customized in 2010 to 128 channels on one carrier to reduce the dead area. The epoxy protection thickness was also reduced: due to the non-zero angle of the light emission from the fibre, the effect of the light spread over multiple channels is now very small. These detectors were employed for test beam and irradiation measurements in 2011 and 2012. An improved package has been defined after discussion with Hamamatsu with smaller dead area on the edge of the chips allowing a gap between two detectors of 250 μm. This package would be suitable for the LHCb fibre tracker and is therefore considered as baseline.

The technology for the 128 channels devices is the standard technology from Hamamatsu MPPC with 55 μm pixel size and 0.25(W)$\times$1.32(H) mm^2 channels, matching the thickness of 5 layers of fibres. The average active area fill factor has been measured to be 55% [22], and leads to a photon detection efficiency (PDE) of 30%, at nominal operation voltage, which is consistent with the standard detectors with the same pixel size [22], [23]. The nominal operation voltage of these detectors is only 1.2 V above the break down voltage. A higher bias voltage to increase the PDE can not, or only in a small range, be used for the irradiated detectors since the dark count increases linearly, and the x-talk and the after-pulsing even quadratically with the over voltage. With the current detector a good gain uniformity was reached, a channel individual bias voltage adjustment in the range of 1 V will suffice to equalize the gain for all channels.

To increase the PDE several modifications have been tested with very good results. The quenching resistors are replaced with metal film resistors which can increase the fill

[2] The VATA64 chip offers a readout with setting 50ns which has a pulse shape that is about 8 times slower than the LHCb requirement. The detailed discussion on this can be found in the note [21]

[3] The x-talk between channels is small and dominated by the one due to the overlapping fibre structure.

factor for the 50 μm pixel size to 80%. Moreover with the change to metal film quench resistor the temperature dependence of the pixel recovery time will be largely reduced and become negligible. The pixels are optically isolated with trenches, reducing the x-talk from currently 10% down to 0.2% and a reduction of after-pulsing has also been achieved. It can also be envisaged to produce samples with higher quench resistor values for further reduction of the after-pulsing. The reduction of x-talk and after-pulsing can allow to increase the over-voltage and therefore gain on the PDE, for an estimation see the simulation section in this document (Sec. 4.4.1). The quoted numbers for the detector improvements are from private discussion with Hamamatsu.

Standard samples will be made available by March 2013 and the 128 channel customized detectors by the end of 2013.

4.2 Detector R&D with KETEK

In 2011, KETEK developed a new structure of SiPM pixels with high fill factor. The prototypes of the 50D-adv type manufactured for the CMS HCAL upgrade with pixels of $50 \times 50 \mu m^2$ reached a fill factor of 68% and PDE >55% at a wavelength of 410 nm [24]. Another advantage demonstrated with this SiPM was a large range of stable operation $V - V_{breakdown} > 10V$. In the same year LHCb started an R&D project with KETEK to develop SiPM multi-channel arrays for the SciFi project. The first main goal was to produce 32-channel arrays with a geometry approaching the final one and improved basic parameters: high fill factor >70%, PDE optimized for 475 nm, minimized x-talk. Furthermore, a fast recovery time of the pixels (about 100 ns) was requested. In addition to the KETEK standard pixel structure, also new structures with improved sensitivity to green light were developed. Those have the additional advantage of a smaller pixel capacitance and provide therefore a faster recovery time of the pixel after discharge. On the other hand, the modified structure leads to an increased breakdown voltage V_{BD} and a larger temperature coefficient $\mathrm{d}V_{\mathrm{BD}}/\mathrm{d}T$.

A further development concerns the introduction of trenches between pixels and/or channels in order to reduce optical x-talk. In view of the incomplete understanding of the radiation tolerance of SiPMs, the experimental comparison of different structures will give new insight for future developments.

The channel geometry of the KETEK 32-channel prototypes was designed to be consistent with the existing multi-channel arrays of Hamamatsu mentioned above. The precise channel size is 0.25×1.32 mm^2. In order to improve the fill factor, the pixel size was increased to $65 \times 67.5 \mu m^2$. The total number of pixels for one channel is $22 \times 4 = 88$. The design allows stitching of chips by sacrificing just one channel. As there is no dedicated industrial packaging available yet, detector modules for the beam tests were equipped with a custom package. It consisted of a G10 frame filled with optically clear epoxy and, optionally, a thin glass window on top. Studies of the effect of epoxy/glass thickness on detector performance like PDE, x-talk and spatial resolution will provide valuable input for the final design of the package.

Measurements of PDE and x-talk were performed on all KETEK prototypes. The

x-talk is obtained by the well established analysis of the noise counting rate as a function of the applied threshold. In a simplified model, the pulse shape of a single pixel signal is defined by the values of the pixel capacitance, the quenching resistor and the parallel capacitance. For the tested SiPM chips, the slow component contains more than 50% of the total charge. A simple pole-zero shaper allows to reduce the pulse duration to a few ns. For the measurement of the dark count rate of irradiated samples, the use of a fast amplifier and shaper becomes mandatory. This allowed to observe dark count rates of up to 60 MHz/channel.

4.2.1 PDE and cross-talk results

The typical PDE and x-talk dependence on the over-voltage measured for KETEK prototypes is shown in Fig. 20. The x-talk value grows almost linearly while the PDE is close to saturation at 4-5 Volts. The study of structures with trenches between pixels shows a x-talk reduction of up to a factor of 5 (type W2-3A) and more than factor 2 for the type W2-3B. At the same time, the introduction of trenches reduces the fill factor by ∼20%. The different structures are compared by means of the correlation plot 'PDE vs x-talk' shown in Fig. 20. The versions with trenches provide in general a better performance.

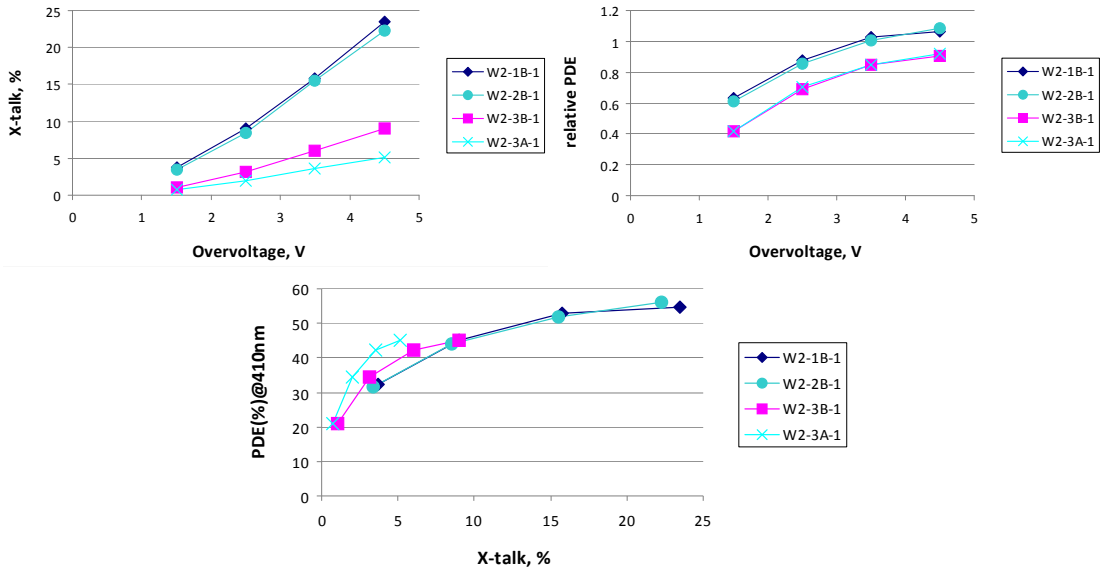

Figure 20: Comparison of PDE and x-talk as function of over-voltage for different SiPM options: W2-1B and W2-2B are versions without and with trenches between channels, respectively; W2-3A and W2-3B have trenches between the pixels and slightly differ in certain design parameters (not disclosed by KETEK).

4.2.2 Effect of trenches between pixels and epoxy thickness on cross-talk

An epoxy layer on top of a SiPM die acts as light guide between adjacent pixels. The magnitude of this optical x-talk phenomenon is expected to depend on the thickness of this layer. In order to estimate this effect, one SiPM (of type W2-3B) with trenches was covered with an epoxy layer of $\sim 200\mu$m thickness. The result of the x-talk measurement is shown in Fig. 21.

The epoxy layer has only a moderate effect on the x-talk and the effectiveness of the trenches is not degraded.

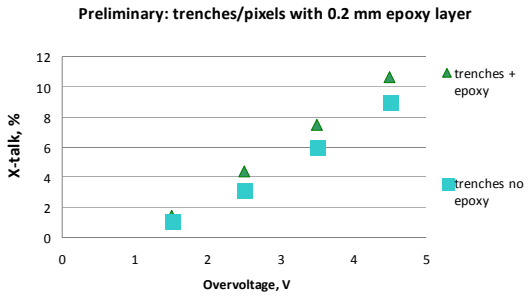

Figure 21: Effect of trenches between pixels on x-talk.

4.2.3 New structures with improved green sensitivity

The detection efficiency for green light is crucial in view of the significant shift of the emission spectrum after irradiation, in particular for long fibres (Sec. 3.3). Placing the p-n junction deeper, as implemented in the new KETEK structure, leads to a higher absorption of green light before the avalanche region. The effect of this change was already experimentally verified (I. Musienko, meeting with KETEK). We plan to perform our own systematic studies of the PDE of the new LHCb specific structures in the near future.

4.3 Radiation damage

The SiPM detectors are known to be strongly affected by charged particle and neutron radiation. The radiation damage results in a strong increase of the dark count rate and a significant decrease of the detector gain. The gain decrease which is suspected to be linked to the saturation from high dark count rate, is strongly reduced when operating at low temperature. Note that a small gain change is nevertheless acceptable for a tracker operation where no precise energy calibration is required.

In the case of the LHCb upgrade the main concern is the damage due to neutrons. The SiPMs being placed outside the acceptance the charged particle flux is at least a factor 100 smaller than neutron flux. A detailed FLUKA simulation was performed to estimate the neutron dose at the top and bottom of the current OT. The detector environment is described in Sec. 2.2.

We have carried out several irradiation tests in the lab and in LHCb. In the lab the neutron irradiation was performed with a Pu-Be neutron source which has neutron energy spectrum similar to the one in LHCb. The neutron dose (expressed in 1MeV neutron equivalent) were measured with calibrated pin diodes.

A first observation is that the SiPM damage is independent from the bias voltage to be present or not during irradiation. We should also mention that during the tests, both in the lab and in LHCb, the neutron irradiation rates were always quite low which excludes a significant rate dependency.

Continuous annealing is taking place during room temperature irradiation at low dose rate. To quantify the effect of annealing, a comparison between a cold (-10°C) and warm (20°C) detector was conducted in LHCb. The study conducted by the Dortmund group showed that the global effect of annealing reduced the dark current by a factor two. Accelerated annealing (with increased temperature) during shut-downs should be envisaged. The precise temperature-time profile will be evaluated at a later time.

Several modifications of the detector design to reduce the dark noise count after irradiation were implemented by Hamamatsu and KETEK. So far only small improvements have been achieved. Ultimately, cooling is the most effective measure to reduce the noise. We observed, that the dark count induced by radiation decreases by a factor 2 every ten degrees. The I-V curves for three detectors with different irradiation levels, tested at different temperatures are shown in Fig. 22. Note that the I-V curves have the same shape for low and high irradiation levels ("low irrad. 0°C" overlaps with "high irrad. -20°C" in Fig. 22).

The radiation damage has shown to be uniform over all channels. In Fig. 23, 128 channels are shown in a histogram at 3 different temperatures. All channels of the device show a similar noise level.

Finally, the x-talk for irradiated and non-irradiated detectors was measured and no significant change due to irradiation was observed. More details can be found in Ref. [21].

In conclusion, the radiation induced damage generates an thermal noise which has an exponential dependance on the temperature. As previously stated, the dark count rate decreases by a factor 2 every 10°C. This is valid over a large range: at least from 25°C down to -100°C. The simulation of the noise cluster rate discussed in Sec. 4.4.1 shows that the necessary operating temperature of the detector depends heavily on the detector x-talk and after-pulse performance. To maintain sufficiently low noise cluster rate and high efficiency, the temperature for the current Hamamatsu detector should be gradually decreased to -40°C at the end life of the LHCb upgrade.

4.3.1 Study of radiation hardness of KETEK SiPMs

Comparative radiation studies were performed for 32-channel KETEK conventional and new structures described above. The equivalent radiation levels corresponded to $0.75\,\mathrm{fb}^{-1}$ (8 TeV) in LHCb and $2.8\,\mathrm{fb}^{-1}$ (8 TeV) for the irradiation with the Pu-Be source. The measurements indicate that the new structures show a 50% reduced dark count rate.

Fig. 24 shows dark count rate (T=22°C), average charge per noise count and x-talk for

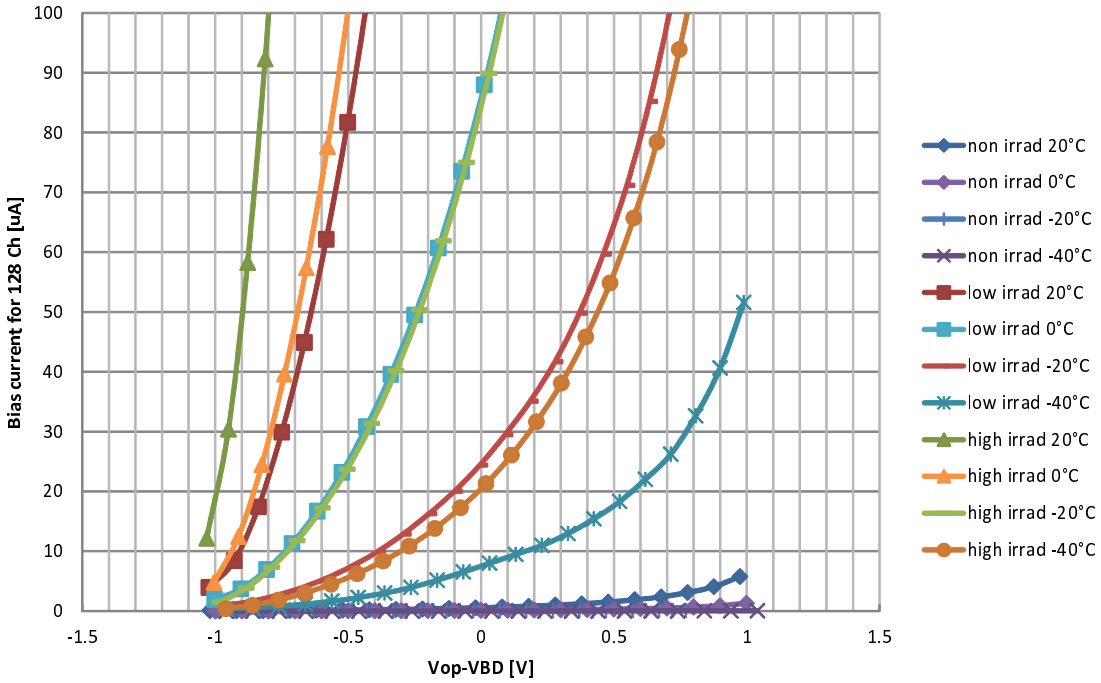

Figure 22: IV-curve of the sum of 128 channels at different temperatures. The operation voltage has been adjusted with 56mV per degree. The shape of the curves of the three detectors indicate that there is no significant change in dark noise due to increased x-talk or after-pulsing (low irradiation $D = 2.5 \cdot 10^{10} n_{\mathrm{eqv}}/\,\mathrm{cm}^2$ ($2\,\mathrm{fb}^{-1}$) and high irradiation $D = 10.3 \cdot 10^{10} n_{\mathrm{eqv}}/\,\mathrm{cm}^2$ ($8\,\mathrm{fb}^{-1}$)). Note that x-talk and after-pulsing become dominant for the dark current above nominal operation voltage (0V in plot) The gain at nominal bias voltage before and after irradiation was measured (photon peak distance) and no change was observed.

a SiPM with a new structure. The 32 channels device was irradiated to the equivalent of $2.8\,\mathrm{fb}^{-1}$. The high degree of uniformity observed in all measured parameters is a strong sign for the control of the new technology. The variability of noise in other SiPMs irradiated in-situ in LHCb to a 4 times smaller value ($0.75\,\mathrm{fb}^{-1}$) was found to be $\sim$2 times higher. This observation may be due to larger statistical fluctuations of the clustering of damages at lower radiation levels. This hypothesis will be verified after further irradiations.

4.3.2 Irradiation with neutron to half and twice the nominal dose

In December 2012 SiPM samples from KETEK (and also from Hamamatsu) were irradiated to $D = 1.5 \cdot 10^{11} n_{\mathrm{eqv}}/\,\mathrm{cm}^2$ and $D = 6 \cdot 10^{11} n_{\mathrm{eqv}}/\,\mathrm{cm}^2$ at the test facility in Ljubljana and Cern PS. For these samples the effect of annealing will also be measured. Unfortunately at the time this note is released the results are not available yet. We shall report on this in the near future.

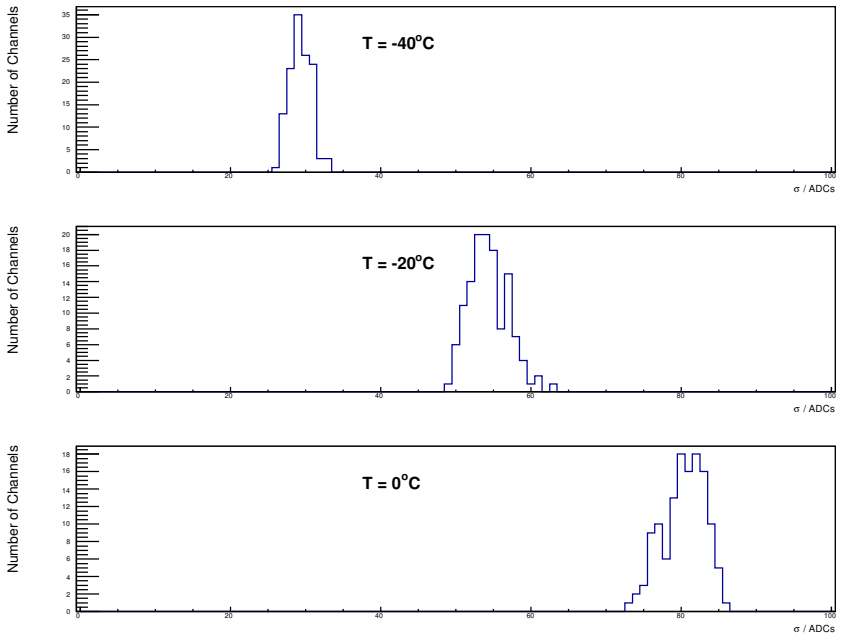

Figure 23: A detector with 128 channels was irradiation to $D = 10.3 \cdot 10^{10} n_{\mathrm{eqv}} / \mathrm{cm}^2$ ($8\,\mathrm{fb}^{-1}$) and the noise plotted in a histogram for different temperatures. The noise is uniformly distributed over all detector channels. The gain of the detector is 50ADC per PE.

4.4 Evaluation of noise cluster rate

A large number of parameters influence the noise behaviour of the SiPM and need to be studied in order to control the noise cluster rate. We have build a computer model which includes the effects from temperature, over-voltage, irradiation, x-talk, after-pulse, detector pulse shape and electronic shaping, as well as the clustering algorithm which was developed for the analysis of test beam data. The model has been verified to predict the dark noise spectrum at different temperatures and different pulse shaping and excellent agreement with data was obtained. The validation of the model is given in the supporting note [21].

The signal in the SciFi detector is typically distributed over two or three detector channels. In the clustering algorithm, after an average common mode subtraction, seed channels are selected above a threshold (typically 2.5 or 3.5 PE). Neighbouring channels above a "neighbouring threshold" ($\sim$1.5 PE) are subsequently included in the cluster. Only clusters exceeding a total cluster sum ($\sim$ 4.5 to $\sim$5.5 PE) are considered as signal clusters. The most important parameter is the seed threshold which is indicated in the plots. The noise cluster rate depends on chosen threshold values, which can be varied in order to understand the effect of noise. The noise cluster rate f_C is defined as the

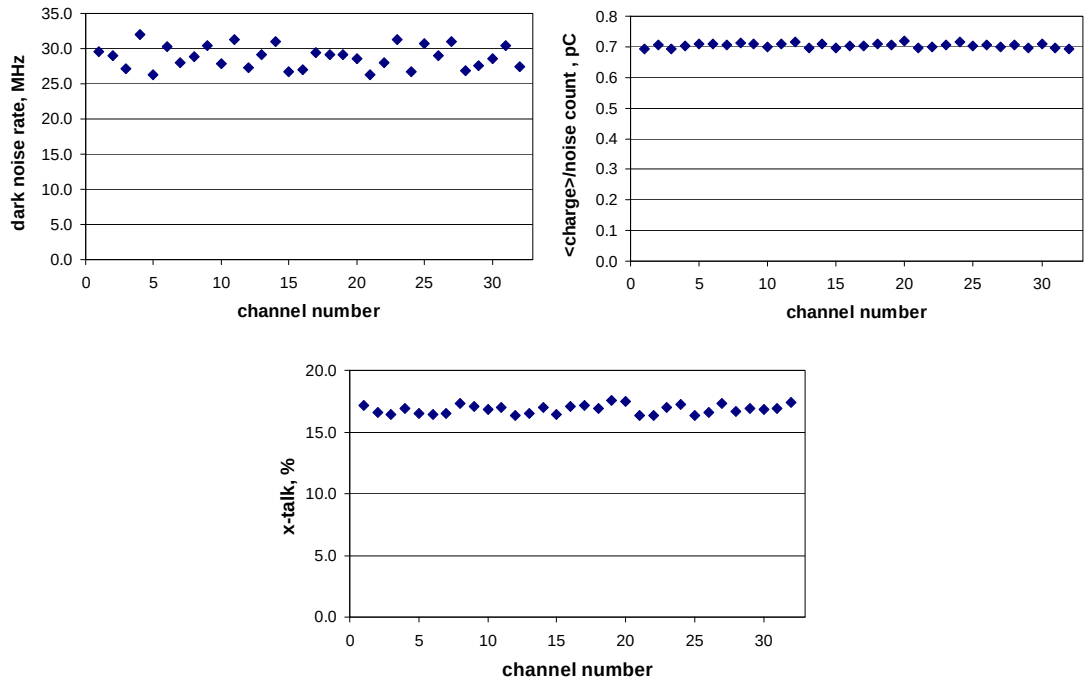

Figure 24: Dark count rate (T=22°C, average charge per noise count and x-talk for 32 channels of a SiPM with new structure after irradiation equivalent to 2.8 fb^{-1}. All measured parameters show a high degree of uniformity.

frequency of noise clusters for a 128 channel detector module and is given by:

$$f_C = f\left(f_P(\Delta V, T, Dose), A(th_{seed}, th_{neigh.}, th_{sum}), p_{x-talk}(\Delta V), p_{after}(\Delta V), \int^{\Delta t}\right) \quad (1)$$

f_P Iis the primary noise rate. It is the thermal noise generated without x-talk and after-pulsing, it increases linear with the over voltage ΔV, depends on the temperature T and the radiation dose received.

A is the clustering algorithm combining single channels into clusters. The most important parameters are the seed, the neighbouring, and the sum thresholds.

p_{x-talk} is the probability that a primary noise signal produces via x-talk a second instantaneous noise signal. The x-talk probability increases strongly with ΔV

p_{after} is the probability for a primary noise signal to produce an after pulse. The after-pulse can occur at times much later than the primary noise.

$\int^{\Delta t}$ is the integration and shaping time of the readout electronics (FE). Long integration and shaping increases the noise cluster rate.

The measurements of the noise has been done with three 128 channel detectors simultaneously irradiated but at different levels ($D = 0$, $D = 2.6 \cdot 10^{10} n_{\text{eqv}}/\,\text{cm}^2$, and $D = 10.3 \cdot 10^{10} n_{\text{eqv}}/\,\text{cm}^2$). The temperature was varied between 20°C and −40°C and the bias voltage was set at several points around the nominal operation voltage. The seed threshold was varied in the analysis to measure the cluster noise rate.

The readout electronics that is used for these measurements is based on the chip VaTa64HDR16-V2R1 [20] . The chip has unfortunately a much slower integration and shaping time then required by the LHCb readout. The timing of the fastest setting is 8 times slower than the requirements for a 25 ns shaping with remainder of less than 25% as it was employed for the current IT readout [25]. A longer shaping time produces a large overlap of single noise pulses which are detected as noise clusters.

4.4.1 Cluster noise simulation results

The noise spectrum generated by the simulation model for −40°C, of an irradiated detector ($8\,\text{fb}^{-1}$) is shown in Fig. 25 on the left. On the right plot, the cluster noise rate simulated for slow shaping (50 ns) and fast (LHCb like) shaping at −20°C and −40°C is shown. The simulation shows that the detector irradiated to the level of $8\,\text{fb}^{-1}$ could be operated at −20°C with a threshold of 2.5 PE seed cut for a noise cluster rate below $f_C = 2$ MHz.

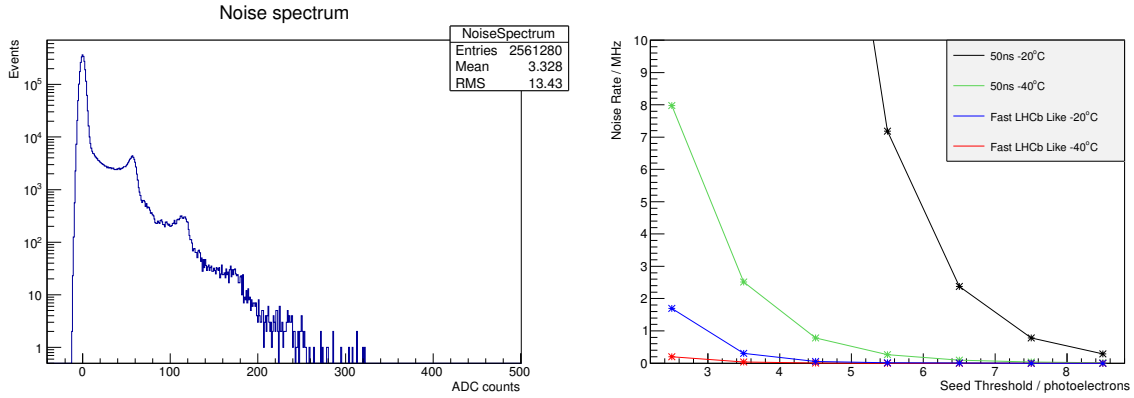

Figure 25: On the left a simulated noise spectrum assuming −40°C, $8\,\text{fb}^{-1}$, and a fast shaping time. On the right the noise cluster rate obtained from the simulations as a function of the seed threshold for both fast and slow shaping time and two cooling temperatures. Note that the noise cluster rate is defined as the frequency of noise clusters in a 128 channel SiPM module.

4.4.2 X-talk and after-pulsing

In Fig. 26 the x-talk probability was changed in the simulation over a large range. Only x-talk between pixels are taken into account. This is particularly interesting since detectors

with much reduced x-talk will be available in the future. The result for a detector irradiated at $8\,\mathrm{fb}^{-1}$ is shown on the left. To extrapolate by simulation to the radiation level required by the LHCb upgrade ($25\,\mathrm{fb}^{-1}$) [4] the primary noise was increased proportionally to the radiation dose.

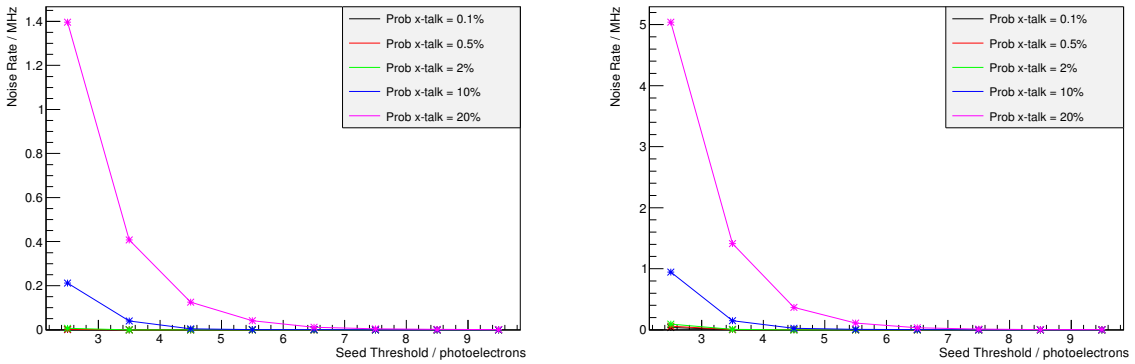

Figure 26: The dependency of the cluster rate on the x-talk for a detector at $8\,\mathrm{fb}^{-1}$, $-40°\mathrm{C}$ is shown on the left. The projection to the full lifetime of the experiment $25\,\mathrm{fb}^{-1}$, $-40°\mathrm{C}$ is given on the right.

The simulation shows that the noise cluster rate is very sensitive to the x-talk. For a fully ($D = 25\,\mathrm{fb}^{-1}$) irradiated sensor at $-40°\mathrm{C}$ a x-talk above $\sim$5% dominates the effects over the dark noise.

Increased after-pulse probability can also contribute to the noise cluster rate. In Fig. 27 the noise cluster rate is plotted for different values. After-pulses are less effective to create noise clusters because they can take place at full amplitude only after the recovery time of a pixel. A fast shaping time will efficiently reduce this effect.

4.5 Cluster size distribution

The cluster size depends mainly on the ratio of the width of the detector channel and the fibre diameter. Other factors can modify the size, in particular the inclusion of noisy channels. Cluster size distributions have been obtained from data recorded in tests in beam. The plots in Fig. 28 show some results. The majority of the clusters are 2 or 3 channel wide and only a small increase can be observed due to tilted tracks.

The cluster distributions have been recorded with non-irradiated detectors and with a detector irradiated at $2\,\mathrm{fb}^{-1}$, operated at a temperature of $-15°\mathrm{C}$. This situation is comparable to a detector irradiated at $11\,\mathrm{fb}^{-1}$ but working at $-40°\mathrm{C}$. Moreover, from

[4] The expected radiation for the detectors after the full life time of the experiment is equivalent to $25\,\mathrm{fb}^{-1}$ taking into account reduction of the radiation by a factor 2 by neutron shielding around the detectors.

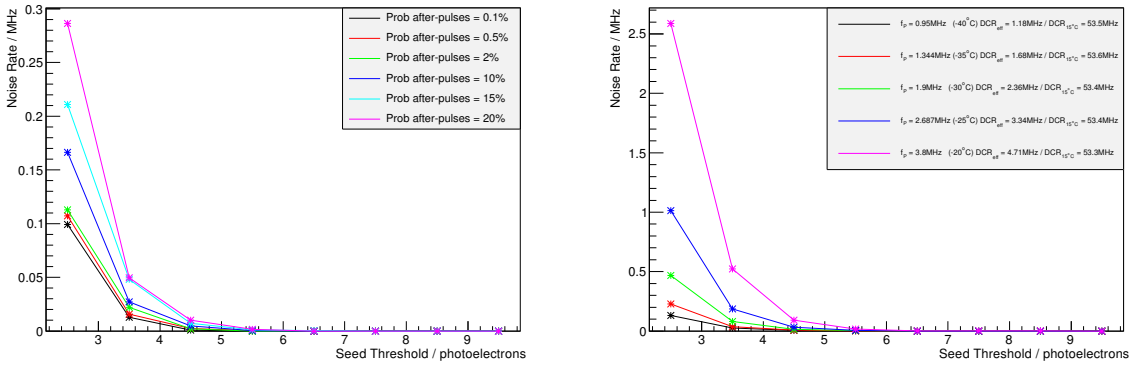

Figure 27: The influence of the after pulse probability is given in the left graphs for a detector irradiated to $8\,\mathrm{fb}^{-1}$ and operating at $-40°$C. On the right side, for a x-talk=10%, after-pulse=15% the noise rate is given for different temperature (the calculated dark count rate is also given). The different temperature effects are obtained by changing the primary noise frequency f_p as indicated in the figure.

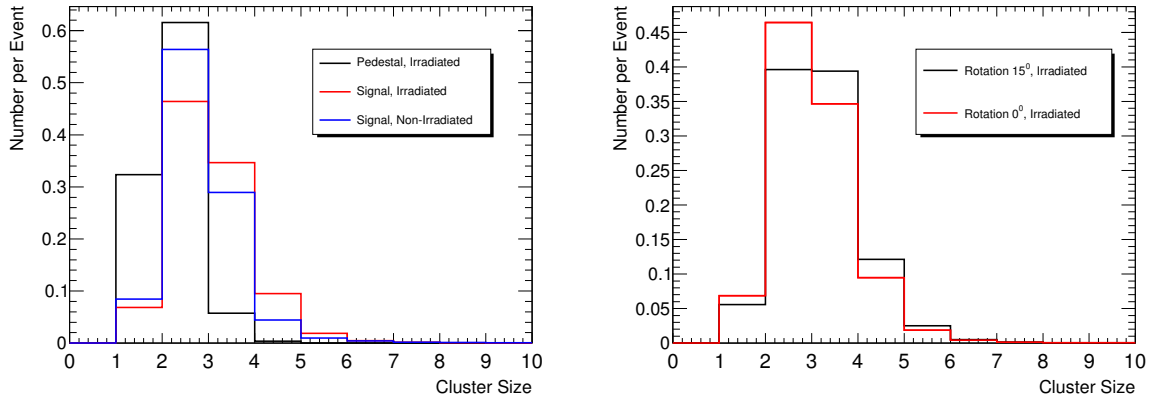

Figure 28: The cluster size distribution for perpendicular tracks are shown in the left hand side plot. The cluster size increases with irradiation due to the noise in neighbouring channels. In the right plot the same is given for an irradiated detector with two different angles. With an angle of 15° the cluster size is slightly increased. Irradiation is equivalent to $2\,\mathrm{fb}^{-1}$ and the temperature was set to $-15°$C. The clustering algorithm used the standard threshold settings $A(th_{seed}, th_{sum}, th_n) = A(2.5, 4.5, 1.5)$. The difference in the cluster size between signal and noise (pedestal) clusters will be used as an input to a neural network to improve the noise cluster rejection.

simulation we know that, normalized to a fast shaping time, these results should correspond to a detector irradiated well beyond the dose expected at the end of the LHCb lifetime.

4.6 Hit detection efficiency and spatial resolution

The detection efficiency is affected by the signal to noise ratio. The signal from a single particle is spread over several detector channels, the clustering algorithm gather the channels and build a cluster with a total amplitude S. The amplitude recorded in a channel has two components: the signal due to incident photons and the one due to the noise, mainly x-talk and after-pulses. The MIP (signal) is defined here as the most likely value of the S distribution, p_S. p_S depends in particular on the light yield of the fibre module and on the detector PDE. To suppress noise clusters, a cut has to be applied which is a source of inefficiency. An illustration of this can be found in Ref. [22] where a value of 1% inefficiency was found.

The spatial resolution was measured and compared to simulation for the proposed geometry of the detector. The centre of gravity of the cluster is used to define the hit position. In Ref. [22] the test beam results show that the detector spatial resolution is better than 60μm for a value of $p_S > 15$ PE. Note that this condition is also required to achieve a detection efficiency of about 99%.

4.6.1 Simulation of the hit detection efficiency

In a dedicated stand-alone simulation (not Geant4 based) the signal of a MIP can be generated and distributed over several channels according to the geometry of the channels and fibre layers. Depending on p_S and the thresholds applied in the clustering algorithm, the hit detection efficiency can be calculated. The MIP value, p_S, depends on the light yield of the fibre module and the detector PDE. This simulation combining signal and noise generators provides a detailed understanding of the efficiency versus noise cluster rate as a function of the overall light yield. Preliminary results are already available but validation by comparison with the data is ongoing. The results of this study will allow to determine the minimum requirements on the overall light yield to obtain the required detector performance over the lifetime of the experiment.

4.6.2 Long module light yield in test beam

A 2.5 m long prototype module has been manufactured for tests purpose [26]. The module is made of 5 staggered layers of Kuraray SCSF-78MJ fibres glued together. The 2.5 m long fibre module with a far end mirror, was placed in the test beam in 2012. The results on the over all light yield (fibre module and detector) show that with the Hamamatsu detector at nominal gain, particle at the far end, the p_S value is 11 PE. For the KETEK detector at the same condition the light yield is 15 – 20 PE depending on the gain.

The light yield of the fibre module in the test beam is for non-irradiated fibres. A loss of 40% indicated in Fig. 17 is expected due to radiation damage and therefore the highest possible PDE of the detector is needed for the compensation of this loss.

In conclusion, for the Hamamatsu detectors to be a viable option, a significant increase of the PDE is required. Future tests will show if the proposed modifications on the structure of the detectors provide the desired improvements.

5 Front-End electronics

Many of the existing integrated front-end electronics chips for SiPMs are optimized for calorimeter readout. They provide a large dynamic range, good linearity and channel individual gain adjustment but lack the possibility of a fast sampling and readout.

For the characterization of the SiPM and fibre modules, our collaboration uses a chip of this type called VaTa64HDR16-V2R1 [20] . It has a low-noise amplifier and shaper but lacks the speed of the LHCb 25 ns readout which requires a custom design. For the tracker application the dynamic range is small, linearity is less important but the fast signal amplification, shaping, digitization, zero-suppression and transmission are the most challenging aspects.

5.1 Readout electronics

The front-end electronics allows to read out the detector at 40 MHz and to transmit the data at this frequency to the data acquisition system based on a cluster of few thousands of computers. The readout scheme is shown in Fig. 29.

The optical signal generated by the scintillating fibre is converted by a SiPM into an electrical signal. The dynamic range for the measurement of up to 3 MIP signal requires a dynamic range of 1 to 30 photons and a signal-to-noise ratio of about 10 to guarantee a good noise suppression. As the particle impact point is determined by the centre of gravity of the hit cluster, a good position resolution requires each channel amplitude to be recorded with at least a 6 bit resolution.

Thus the signal digitization requires a custom designed ASIC with 128 6-bits ADC leading to 40 MS/s. This means a chip generates 31 Gb/s of data. A development made by CERN, called GBT, with an output rate of 3.2 Gb/s will be used to transfer the data to the acquisition system thanks to optical fibres. Sending the whole data from the ADC to the counting room is too expensive and power consuming. Hence, the introduction of data compression (including zero suppression) electronics on the detector is required.

The expected maximum mean occupancy for a SiPM is around 3 to 4%. Usually a clusterization algorithm is used to suppress data inside a FPGA, but to send 31 Gb/s from an ASIC to a FPGA is already very challenging and a lot more expensive. It is why we propose to compute the barycentre of the track directly within the front-end ASIC chip.

5.2 The ASIC

The low-Power ASIC for the sCIntillating FIbres traCker (PACIFIC) will include all the elements to process the data from one SiPM. Hence, it will have the same granularity (128ch/chip).

It will have to be low power (1W/chip or 8mW/channel) and radiation tolerant. The chip will use the IBM 130 nm technology. The next subsections are dedicated to its 3 processing parts :

1. the amplifier and the shaping;

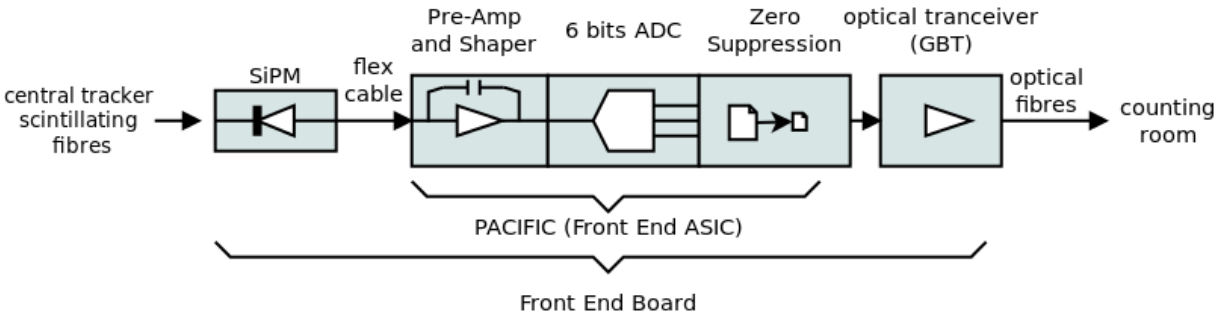

Figure 29: The central tracker front-end readout electronics

2. the 6 bits ADC running;

3. the digital processing.

Several options are considered for the analog and the digital processing. One solution uses a standard flow with a gated integrator followed by a 40MS/s ADC. This option has the advantage of simplicity but the tails of the processed signal can be lost. Another solution is based on a complex digital processing involving deconvolution algorithms with a fast ADC. For the sake of simplicity, this document is focused on the first option.

The SiPM need a fine control on their bias voltage. This will be done using a embedded DAC in the PACIFIC chip.

Finally, the slow control interfaces (I^2C, JTAG...) and the synchronisation with the experimental system will not be discussed here but will be obviously part of the chip.

5.3 The shaping and the gated integrators

The shaping, illustrated in Fig. 30, is based on a gated integrator (GI) digitalized with a 40MS/s ADC. The integrator is triggered directly by the experiments 40MHz clock. The signal acquisition must be as fast as possible, so a low input impedance amplifier is needed to assure short recovery time. The amplifier is followed by a differentiator in order to reduce the pulse width. The GI is doubled to take into account two consecutive hits on the same SiPM channel and thus avoid any dead time. The sub-channel selection is made through a demultiplexer.

The constraints on the shaping are summarized in the following table:

Detector type	128 channels MPPC
Signal/Noise ratio (for 1 MIP)	> 10
Detector capacitance	$< 20pF$
Input impedance	$\approx 20\Omega$
Dynamic range	3MIP ($\approx$ 50/60 firing cell)
Power consumption (full chip)	$< 1W$
Allowed dead time	no

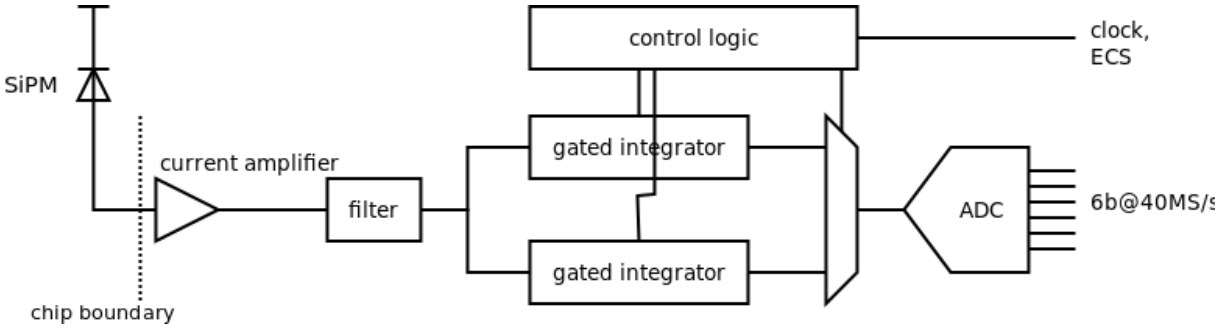

Figure 30: Analog readout

5.4 The ADC

An ADC running at 40MS/s is required for the digitization of the analog signal from the gated integrators. It needs to be 5 or 6 bits in order to obtain a resolution on the particle track that is better than $72\mu m$ with the interpolation algorithm.

The constraints on the ADC are summarized in the following table:

Number of bit	6 bits
Sampling rate	40 MS/s
Power consumption (full chip)	$< 1W$
Allowed dead time	no

5.5 The digital processing

The first task of the digital processing will be to adjust the gain and the pedestal of the digitized data. This step allows to fit the channels' outputs on the same scale.

Two running mode are then foreseen. The first one is for monitoring and debugging purpose. It is called non-zero suppressed (NZS) as the full data coming from the ADC is sent to the GBT. This mode can not be used in normal operation as a chip generate 31Gb/s of data on a 3.2Gb/s link. For this purpose, a second mode called zero-suppression (ZS) is developed. A data compression is applied to the data using hit finders and clusterization procedures. In a first step, the seeding strips are found using a programmable thresholds and neighbouring hits are combined into a cluster. In the second step, the cluster position is calculated by computing the barycentre using a weighted average with a 2-bit inter-channel precision (i.e. 75 μm). Finally, the data are packed to send only the cluster position to the GBT on a 16-bit word.

5.6 Conclusion

The readout chip presented in the last subsection use well-known and simple techniques for the chip design. This solution will work if the signal coming from the SiPM can be shaped to fit in a 25ns windows.

Hence, in the meanwhile, we study more complex digital processing (as deconvolution algorithms) in order to be able to fill the requirement by relaxing the timing constrains on the SiPM signals.

6 Performance Expectation from Simulation

The role of the SciFi detector is to measure tracks after the magnet, mainly to measure the momentum of long tracks, but also to reconstruct in stand-alone tracks that were not seen in the Velo, in particular for K^0 and Λ that decay after the Velo. A first version of the reconstruction code exists and was used to assess the effect of possible detector degradation as discussed in the rest of this document.

The effect of the increased noise rate has been estimated, and we conclude that a rate of 2 MHz per SiPM module (128 channels) after zero suppression will not affect sensibly the performance of the reconstruction of tracks with the SciFi tracker [27].

The effect of ageing fibres is very localized, as it affects seriously only the last 10 to 20 cm of fibres near the horizontal plane in the central region. With a mirror at the end of the fibre, the amount of light received by the SiPM varies by 30% on a non-irradiated fibre according to the position along the fibre. In the central fibres, this becomes about 40%, after irradiation and this is not thought to create serious inefficiencies.

A more detailed study is being pursued, with a proper simulation of the noise according to irradiated SiPM measurements, realistic signal processing, clustering and zero suppression, to confirm these first estimations of the effect of radiation on the performance of the detector. Our current understanding is that the global degradation will be very small.

7 Engineering and Quality Control Aspects

7.1 Module production

One detector layer consists of five layers of scintillating fibres to achieve a sufficiently high light yield. These layers are shifted by half a pitch to achieve a dense packing. The pitch has to be larger than the nominal diameter of the fibre due to fluctuations (thickness varies by 6 μm (RMS) [28]).

The production method for a fibre ribbon is inspired by the production of fibre modules (860 mm long) by RWTH Aachen for the PEBS experiment [28]. To produce 2.5 m modules a new machine has been developed and built by TU Dortmund. Due to the fact that no fibre ribbon has been built with this machine (Fig. 31) so far (expected for spring 2013), all following numbers are taken from measurements by the Aachen group. The fibre is wound on an aluminium cylinder. The position is set by a thread in the surface for the first layer and by the fibres of the previous layer from the second layer upwards. The glue is placed constantly on the single fibre before. The positioning accuracy of the fibres depends on the accuracy of the thread and the thickness fluctuations of the fibres. It has been shown that the fibres can be placed with an accuracy of 25 μm next to each

other [28] and each fibre follows a straight line with deviations smaller than 60 μm over a length of 860 mm [29]. First simulations show that it is desired to achieve a accuracy below 100 μm [30], over 2.5 m long fibre ribbons.

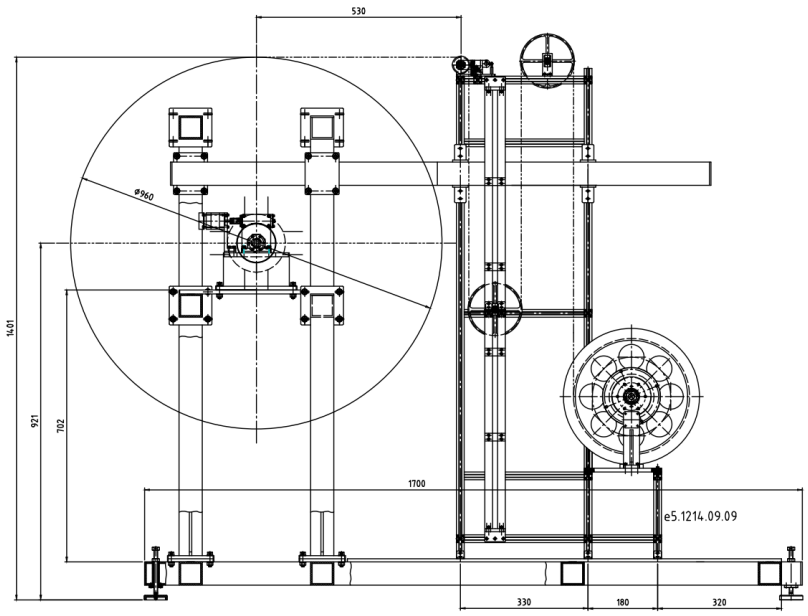

Figure 31: Fibre ribbon winding machine developed by TU Dortmund.

The fibre ribbon is cut at a designated position after the glue mainly cured. A controlled variation of the tension on the fibre during winding helps to achieve a flat ribbon. The remaining tension has to be controlled by the support structure. A first design of the support has started (situation December 2012). The manufacturer of the Aachen support (an external company) has the possibilities to scale it to a length of 2.5 m. The stiffness of the support should guarantee random variations in the z-direction of below 300 μm [30].

7.2 Fibre quality control

The quality of the delivered fibre is subject to variations. Due to the fragile structure, cracks can occur easily. These can harm the light transport. A machine has been developed which checks the fibre for lateral light losses and defects in light guidance [31, 32]. It is part of the current research to define thresholds to achieve a good compromise between quality and rejects.

The manufacturing process of the fibre causes a varying diameter. The quality control machine measures the diameter in two planes to check whether it is suitable for the production [33]. An additional mechanical veto recognises small blobs which could destroy the fibre assembly during the module winding process.

8 Conclusion

A scintillating-fibre detector is considered for the upgrade of the LHCb downstream tracking stations. The full height of the acceptance region would be covered by two sets of 2.5 m long fibres, read out outside of the acceptance with Silicon PhotoMultipliers (SiPM).

The required detector performance includes high efficiency, resolution at the level of 60–100 μm, low budget material in the acceptance, and a 40MHz readout system, while the detector must be resistant to radiations accumulated during the lifetime of the LHCb upgrade. In this document, we presented the scintillating-fibre detector performance, with a strong focus on the radiation damage, and made projections for the performance after LHCb has collected an integrated luminosity of $50\,\text{fb}^{-1}$, corresponding to 10 years of data taking at $5\,\text{fb}^{-1}$/yr.

Scintillating fibres with diameter of 250 μm, of type Kuraray SCSF-78MJ, have been irradiated up to ≈ 22 kGy. We find that the primary scintillation and the wavelength shifting mechanism appear to be unaffected. However, a significant reduction of the optical absorption length is observed. A good description of our data is obtained with a model relating the observed damage and the dose. We use this model in conjunction with the FLUKA-simulated dose at the location of the LHCb tracking stations to predict the loss in light yield due to absorption after irradiation. We find that the loss in light yield after irradiation is 40% for the most exposed fibre modules, which can be designed for replacement. We also find that with the use of a mirror at the end of the fibre, a significant fraction of the light is recovered from the region most exposed to radiation damage.

SiPM detectors are being developed in collaboration with two companies, Hamamatsu and KETEK. Both provide multichannel arrays, with 250 μm pitch, but with different properties, such as geometrical fill factor, quantum efficiency, breakdown voltage, and geometric structures such as trenches between pixels and channels. The tracking performance is driven by the ratio of the signal over the noise cluster rate, which should be maximized while keeping the noise cluster rate below 2 MHz (per 128-channel SiPM).

To estimate the noise performance of the SiPM in the LHCb upgrade environment, we used a combination of measurements and simulation. The simulation was tuned and validated on a range of parameter values, giving us confidence in its predictive power. From these studies, we find that a combination of low operation temperature (-40°C to -20°C), short integration time (25 ns), and shielding of the SiPMs from neutron damage, allows maintaining the necessary low noise level, with the existing detector technology, and over the nominal lifetime of the experiment.

The photon detection efficiency was studied with a 2.5 m long fibre module placed in a test beam at the CERN SPS. The results show that 11 (Hamamatsu) to 20 (KETEK, high gain) photons per charged particle are detected, depending on the type of SiPM. Together with the projected light attenuation in the fibres after irradiation, we conclude that only the high end of this range, near 20 photons, is acceptable.

However, we can also rely on expected performance improvements in the near future. For example, the addition of trenches between pixels in the Hamamatsu SiPM and the use of metal film resistors are announced to help reduce significantly the cluster noise rate

(by reduction of the x-talk), while the over-voltage will be increased for improved gain and photon detection efficiency. We also consider the possibility to use 6, instead of 5, layers of densely packed scintillating fibres, for a gain of 20% on the light yield. These improvements should provide the necessary safety margin for operations in the LHCb upgrade.

A design of the 40 MHz front-end electronics was presented, and we discussed engineering aspects of the construction of long fibre modules with the required accuracy.

Based on the studies presented in this document, we conclude that a tracker for the LHCb detector upgrade can be built with the scintillating-fibre technology, read out with SiPM detectors. The projected performance would fulfil the requirements for the lifetime of the experiment, but with little margin after reaching a delivered luminosity of $50\,\mathrm{fb}^{-1}$. This margin will be significantly increased by expected performance gains from already well defined and scheduled technological improvements.

Acknowledgements

We thank Prof. Dr. Stefan Schael and his team from RWTH Aachen for useful discussions and invaluable advices, Gloria Corti for her help with in situ irradiations and with the simulation, Maurice Glaser and Federico Ravotti (CERN PH/DT) for the irradiation in the PS facility, Ian Mcgill and Alan Honma from the CERN bond lab, Claude David, Miranda v. Stenis (CERN) and Evgeny Chernov for competent technical support, Iouri Musienko, Arjan Heering (CMS), Elena Popova (MEPHY) and Sergey Klemin (TOPEK) for fruitful co-operation on SiPM R&D, Kirill Kachnov (IHEP) for the production of the long fibre module, and Vladimir Cindro (Ljubljana) for the irradiation with reactor neutrons. The research leading to these results has received funding from the European Commission under the FP7 Research Infrastructures project AIDA, grant agreement no. 262025.

References

[1] R. Aaij et al. Letter of Intent for the LHCb Upgrade.

[2] I. Bediaga et al. Framework TDR (FTDR) for the LHCb Upgrade .

[3] B. Beischer, H. Gast, R. Greim, W. Karpinski, T. Kirn, T. Nakada, G. Roper Yearwood, S. Schael, and M. Wlochal. A high-resolution scintillating fiber tracker with silicon photomultiplier array readout. *Nuclear Instruments and Methods in Physics Research Section A: Accelerators, Spectrometers, Detectors and Associated Equipment*, 622(3):542 – 554, 2010.

[4] J.Ranft A. Fasso, A. Ferrari and P. R. Sala. The fluka: a multi-particle transport code, 2005. CERN-2005-10, INFN/TC05/11, SLAC-R-773.

[5] V. Vlachoudis. Flair: A powerful but user friendly graphical interface for fluka, 2009. Proc. Int. Conf. on Mathematics, Computational Methods and Reactors Physics (MandC 2009), Saratoga Springs, New York.

[6] K. H. Buchegger C. Theis. Interactive three dimensional visualization and creation of geometries for monte carlo calculations. *Nuclear Instruments and Methods in Physics Research A*, 562:827, 2006.

[7] M. Karacson N. Lopez March. Radiation studies for the lhcb tracker upgrade. Technical report, EPFL Lausanne, CERN, Switzerland, 2013.

[8] L. Shektman G. Corti. Estimation of induced radioactivity in lhcb to determine the reference waste zoning of the experiment, June 2007. LHCB-2007-097 and EDMS 850261.

[9] Ask et. al. *NIM A*, 568:588, 2006.

[10] A. Braem, A. Folley, J. Gentil, C. Joram, and L. Kottelat. Characterization studies on scintillating fibres. *ATL-LUM-2006-004*, 2006.

[11] W. Busjan, K. Wick, and T. Zoufal. Shortlived absorption centers in plastic scintillators and their influence on the fluorescence light yield. *Nuclear Instruments and Methods in Physics Research Section B: Beam Interactions with Materials and Atoms*, 152(1):89 – 104, 1999.

[12] Z. Papandreou. Performance of 'first-article' scintillating fibres for the gluex barrel calorimeter. Technical Report GlueX-doc-1319, University of Regina, JLab, March 2010.

[13] C. Zorn. A pedestrian's guide to radiation damage in plastic scintillators. *Nuclear Physics B - Proceedings Supplements*, 32(0):377 – 383, 1993.

[14] K. Hara, K. Hata, S. Kim, M. Mishina, M. Sano, Y. Seiya, K. Takikawa, M. Tanaka, and K. Yasuoka. Radiation hardness and mechanical durability of kuraray optical fibers. *Nuclear Instruments and Methods in Physics Research Section A: Accelerators, Spectrometers, Detectors and Associated Equipment*, 411(1):31 – 40, 1998.

[15] Louis Archambault et al. *Medical Physics*, 32:2271, 2005.

[16] S.Bruggisser. Literature study on the radiation damage on KURARAY fibers. LHCb TWiki, September 2012. https://twiki.cern.ch/twiki/pub/LHCb/ScintFiber/FiberSummaryNew.pdf.

[17] Pavel Shatalov Christian Joram, Thomas Schneider. Measurements and radiation tests on scintillating fibres for the lhcb scifi project. Technical report, CERN, Switzerland, 2013.

[18] M. Deckenhoff. Signal shapes and travel time of photons in scintillating fibre. LHCb SciFi fiber specification meeting, 14 November 2012.

[19] Alan D. Bross and Anna Pla-Dalmau. Radiation effects in intrinsic 3hf scintillator. *Nuclear Instruments and Methods in Physics Research Section A: Accelerators, Spectrometers, Detectors and Associated Equipment*, 327(23):337 – 345, 1993.

[20] Inc. (Norway) Gamma Medica-Ideas. Martin Linges vei 25, Snaroya, POB I, N- 1330 Fomebu, Norway, Tel: +47-6782-7171.

[21] E. Gushchin G. Haefeli. Sipm development and performance. (in preparation).

[22] 2007 IEEE Nuclear Science Symposium Conference Record. *Preliminary Results from a Current Mode CMOS Front-End Circuit for Silicon Photomultiplier Detectors*, 2007.

[23] Yuri Musienko. State of the art in sipms, February 2011. SiPM workshop.

[24] CMS Collaboration. Cms hcal upgrade tdr, September 2012. CERN-LHCC-2012-015,CMS-TDR-010.

[25] Beetle 1.3 reference manual.

[26] Construction and performances of a 2.5m long scintillating fiber tracker prototype for the lhcb upgrade. CERN EDMS document 1263350 (to appear soon).

[27] O. Callot. Acceptable noise rate in the sipm of the fibre tracker, 2012. LHCb-INT-2012-033.

[28] G. Roper Yearwood. The development of a high-resolution scintillating fiber tracker with silicon photomultiplier readout, 2010. presented on the Vienna Conference on Instrumentation February 18, 2010.

[29] G. Roper Yearwood. email, 18dec2012, 2012.

[30] O. Callot. Software for ft, 2012. talk at the LHCb Upgrade SciFi Tracker meeting 13Dec2012.

[31] M. Deckenhoff. Entwicklung einer qualitätsanalyse für szintillierende fasern - untersuchungen zur datennahme des sipm-moduls, messverfahren und datenanalyse zur bestimmung von faserparametern, automatisierte regelung der faserspulung. Master's thesis, 2009.

[32] F. Kruse. Entwicklung einer qualitätsanalyse für szintillierende fasern -geant4-simulationen, entwicklung der datennahme, messungen an szintillierenden fasern. Master's thesis, 2009.

[33] S.Swientek. Mechanische belastungen von szintillierenden fasern. Master's thesis, 2010.